

Nodal band-off-diagonal superconductivity in twisted graphene superlattices

Maine Christos,¹ Subir Sachdev,¹ and Mathias S. Scheurer^{2,3}

¹*Department of Physics, Harvard University, Cambridge MA 02138, USA*

²*Institute for Theoretical Physics, University of Innsbruck, Innsbruck A-6020, Austria*

³*Institute for Theoretical Physics III, University of Stuttgart, 70550 Stuttgart, Germany*

The superconducting state and mechanism are among the least understood phenomena in twisted graphene systems. Recent tunneling experiments indicate a transition between nodal and gapped pairing with electron filling, which is not naturally understood within current theory. We demonstrate that the coexistence of superconductivity and flavor polarization leads to pairing channels that are guaranteed by symmetry to be entirely band-off-diagonal, with a variety of consequences: most notably, the pairing invariant under all symmetries can have Bogoliubov Fermi surfaces in the superconducting state with protected nodal lines, or may be fully gapped, depending on parameters, and the band-off-diagonal chiral p -wave state exhibits transitions between gapped and nodal regions upon varying the doping. We demonstrate that band-off-diagonal pairing can be the leading state when only phonons are considered, and is also uniquely favored by fluctuations of a time-reversal-symmetric intervalley coherent order motivated by recent experiments. Consequently, band-off-diagonal superconductivity allows for the reconciliation of several key experimental observations in graphene moiré systems.

I. INTRODUCTION

The fascinating physics [1, 2] of correlated graphene moiré superlattices, such as twisted bilayer (TBG) and twisted trilayer graphene (TTG), has generated extensive efforts to uncover the mysteries of their phase diagrams. Much progress has been made towards understanding their normal-state physics, including the correlated insulating phases [3–18] and the reset behavior [19, 20]; the latter, which is believed to be associated with the onset of flavor polarization, appears in the same density range of and can coexist with superconductivity [13, 19–34]. However, the form and symmetry of the superconducting order parameter and the pairing glue are still unknown, despite significant theoretical efforts [27–30, 33, 35–47].

Tunneling conductance measurements taken within the superconducting state reveal V-shaped density of states (DOS) [48, 49] which can become U-shaped at other electron concentrations [49]. Setting aside the possibility of thermal fluctuations as origin [50], this is most naturally interpreted as a transition from nodal to fully gapped superconductivity. For a consistent microscopic theoretical understanding, this provides the following challenges: (i) electron-phonon coupling—a widely discussed [33, 35–40] pairing mechanism in TBG and TTG—will typically mediate an entirely attractive interaction in the Cooper channel, with leading pairing state that transforms trivially under all symmetries and is thus fully gapped [51, 52]. (ii) Even when the low-energy interactions favor an irreducible representation (IR), e.g., E of C_3 , with nodal basis functions (p - or d -wave), the generically fully gapped chiral configuration wins over the nodal nematic one within mean-field. (iii) Even if we assume that the nodal state is energetically favored, e.g., due to sig-

nificant corrections beyond mean-field [27, 53–55], one is still left to explain why there is a transition to another, fully gapped superconductor upon changing the filling.

In this work, we show that the combination of flavor polarization and the representations of the symmetries in the flat bands of TBG and TTG allow for pairing channels that are completely off-diagonal in the flat bands and that such band-off-diagonal states can naturally reconcile all three key challenges (i-iii). More specifically, we find two distinct band-off-diagonal states: one of them transforms under the trivial representation A of the system's point group C_6 (or one of $A_{1,2}$ of D_6 if we set the displacement field to zero) but can nonetheless have symmetry-protected nodal lines, akin to Bogoliubov Fermi surfaces discussed in [56, 57], see Fig. 1(a-c) for an intuitive visual explanation. The surprising possibility of the existence of such Bogoliubov Fermi surfaces without external magnetic field is unique to twisted graphene systems in that it follows as a direct consequence of both the symmetry and relative flatness of their normal-state bands. The second off-diagonal state transforms under a two-dimensional IR (E_2 of C_6). Its associated chiral state, $E_2(1, i)$, which is favored in mean-field over the nematic one, has the unique property of exhibiting nodal lines or being fully gapped depending on the filling fraction, even when the order parameter is kept fixed. We supplement our general symmetry arguments and phenomenological models with Hartree-Fock (HF) calculations on the continuum model, studying a variety of different pairing mechanisms. We find that nodal band-off-diagonal pairing is favored by the optical A_1 and B_1 phonon modes and by fluctuations of a time-reversal symmetric intervalley coherent (T-IVC) state (the T-IVC state has Kekulé order on the graphene scale [58–60]). Evidence for the former has been provided by a recent photoemission study [61] while evi-

dence for the latter comes from recent STM experiments [7]. Furthermore, also fluctuations of a time-reversal-symmetric sublattice polarized state (SLP+) are attractive in the band-off-diagonal channel (see Table II for a formal definition of the order parameters). We also show that fluctuations of both T-IVC and of a nematic, time-reversal symmetric IVC order [62] favor either the band-off-diagonal A or an E_1 state with band-diagonal components, which may also be nodal; the winner is determined by the relative amount of nematic IVC and T-IVC fluctuations.

II. RESULTS

A. Possible pairing states

Let us begin by classifying the superconducting instabilities in graphene moiré systems in the limit where the low-energy bands are spin polarized but allowing for multiple bands. We denote the spinless low-energy fermionic creation operators by $c_{\mathbf{k},\alpha,\eta}^\dagger$ with momentum \mathbf{k} in valley $\eta = \pm$, and of band index α labeling the upper ($\alpha = +$) and lower ($\alpha = -$) quasi-flat bands. As a result of two-fold rotational symmetry, C_{2z} , along the out-of-plane (z) direction or effective spinless time-reversal symmetry, Θ , the non-interacting band structure $\xi_{\mathbf{k},\alpha,\eta}$ obeys $\xi_{\mathbf{k},\alpha,\eta} = \xi_{-\mathbf{k},\alpha,-\eta} \equiv \xi_{\eta,\mathbf{k},\alpha}$ and intervalley pairing is expected to dominate. A general pairing order parameter in the inter-valley channel couples as

$$\mathcal{H}_p = \sum_{\mathbf{k},\eta=\pm,\alpha,\alpha'} c_{\mathbf{k},\alpha,\eta}^\dagger (\Delta_{\mathbf{k},\eta})_{\alpha,\alpha'} c_{-\mathbf{k},\alpha',-\eta}^\dagger + \text{H.c.}, \quad (1)$$

where the order parameter $\Delta_{\mathbf{k},\eta} = -\Delta_{-\mathbf{k},-\eta}^T$ is a matrix in band space. The physical spin texture of the superconductor is entirely determined by the form of the underlying normal state's polarization: if the spins are aligned in the two valleys, the superconductor is a non-unitary triplet, while anti-alignment [24, 28] leads to a singlet-triplet admixed state [13, 27, 28]. In both cases, all of the following states are well defined, with the aforementioned spin structures and symmetries given by appropriate combinations of spinless operations and spin rotations (see Appendix A1).

We will classify the pairing states according to the irreducible representations (IRs) of the system's point group D_6 , which is generated by six-fold rotations (C_{6z}) along the z axis and two-fold rotation symmetry (C_{2x}) along the in-plane x axis. Note a displacement field ($D_0 \neq 0$) breaks the in-plane rotations leading to the point group C_6 . Importantly, all IRs of D_6 and C_6 are either even or odd under C_{2z} . Choosing the phases of the Bloch states such that C_{2z} acts as $c_{\mathbf{k},\alpha,\eta} \rightarrow c_{-\mathbf{k},\alpha,-\eta}$, it holds

$$C_{2z} : \Delta_{\mathbf{k},\eta} \longrightarrow \Delta_{-\mathbf{k},-\eta} = -\Delta_{\mathbf{k},\eta}^T. \quad (2)$$

TABLE I: Summary of pairing states in spin-polarized flat bands. Here $\chi_{\mathbf{k}}$ ($\hat{\chi}_{\mathbf{k}}$) is a real-valued (real and symmetric 2×2 matrix-valued) MBZ-periodic function invariant under C_{3z} . Furthermore, $X_{\mathbf{k}}$ and $Y_{\mathbf{k}}$ ($\hat{X}_{\mathbf{k}}$ and $\hat{Y}_{\mathbf{k}}$) transform as x and y under D_3 , generated by C_{3z} and C_{2x} , while also being real (and symmetric). The third column indicates the type of nodes—line (ln), point (pt), or none (n)—on a generic Fermi surface for sufficiently small/large order-parameter magnitudes; options separated by “or” indicates that this depends on the normal-state band splitting, see main text. The last column shows which states merge when $D_0 \neq 0$, reducing the point group from D_6 to C_6 .

IR of D_6	$\Delta_{\mathbf{k},\eta} = -\Delta_{-\mathbf{k},-\eta}^T$	nodes	IR of C_6
A_1	$\sigma_y \chi_{\eta,\mathbf{k}}, \chi_{C_{2x}\mathbf{k}} = -\chi_{\mathbf{k}}$	ln/pt or ln	A
A_2	$\sigma_y \chi_{\eta,\mathbf{k}}, \chi_{C_{2x}\mathbf{k}} = \chi_{\mathbf{k}}$	ln/n	A
$E_2(1,0)$	$\sigma_y Y_{\eta,\mathbf{k}}$	ln/ln or pt	$E_2(1,0)$
$E_2(0,1)$	$\sigma_y X_{\eta,\mathbf{k}}$	ln/ln or pt	$E_2(1,0)$
$E_2(1,i)$	$\sigma_y (X_{\eta,\mathbf{k}} + i Y_{\eta,\mathbf{k}})$	ln/ln or n	$E_2(1,i)$
B_1	$\eta \hat{\chi}_{\eta,\mathbf{k}}, \sigma_z \hat{\chi}_{C_{2x}\mathbf{k}} \sigma_z = \hat{\chi}_{\mathbf{k}}$	n	B
B_2	$\eta \hat{\chi}_{\eta,\mathbf{k}}, \sigma_z \hat{\chi}_{C_{2x}\mathbf{k}} \sigma_z = -\hat{\chi}_{\mathbf{k}}$	pt	B
$E_1(1,0)$	$\eta \hat{X}_{\eta,\mathbf{k}}$	pt	$E_1(1,0)$
$E_1(0,1)$	$\eta \hat{Y}_{\eta,\mathbf{k}}$	pt	$E_1(1,0)$
$E_1(1,i)$	$\eta (\hat{X}_{\eta,\mathbf{k}} + i \hat{Y}_{\eta,\mathbf{k}})$	n	$E_1(1,i)$

This immediately implies that the pairing states in all IRs even under C_{2z} (A_1, A_2, E_2 of D_6) must be anti-symmetric in band space and, thus, entirely band off-diagonal, whereas the order parameters of the other IRs (B_1, B_2, E_1) are symmetric and can contain both band-diagonal and band-off-diagonal components. While superconducting order parameters with finite band-off-diagonal components are rather common in multi-band systems, the existence of pairing states that are constrained to be entirely band-off-diagonal is rather unique and follows from the combination of C_{2z} symmetry and the spin polarization in the normal state. Importantly, this is unaffected by strain or nematic order breaking C_{3z} as long as C_{2z} remains, which guarantees that there are IRs with entirely band-off-diagonal order parameters.

Choosing the phase conventions of the Bloch states such that C_{2x} and C_{3z} act as $c_{\mathbf{k},\alpha,\eta} \rightarrow (\sigma_z)_{\alpha\alpha'} c_{(k_x,-k_y),\alpha,\eta}$ and $c_{\mathbf{k},\alpha,\eta} \rightarrow c_{C_{3z}\mathbf{k},\alpha,\eta}$, respectively, the resulting candidate order parameters are summarized in Table I. Note that a momentum-independent representation of C_{2x} must be σ_z due to the bands' eigenvalues at the Γ -M line, which in turn are connected to the topological obstruction of the flat bands [63]. The reality (Hermiticity) constraint in Table I on χ , X , and Y ($\hat{\chi}$, \hat{X} , and \hat{Y}) comes from the residual spinless time-reversal symmetry Θ of the normal state [64, 65]. The two two-dimensional IRs $E_{1,2}$ are each associated with three pairing states—two nematic phases $E_{1,2}(1,0)$, $E_{1,2}(0,1)$ and one chiral

state $E_{1,2}(1, i)$.

B. Spectral properties

We here have the rather unique situation that there are pairing channels, associated with the IRs $A_{1,2}$ and E_2 , where the pairing is constrained by C_{2z} to be entirely band off-diagonal. One immediate very unusual consequence is that the superconducting order parameter transforming under the trivial representation (A_1) has a symmetry-imposed line of zeros along the Γ -M line, and hence a nodal point in the spectrum. This is related to the topology-induced non-trivial representation of C_{2x} in band space. We refer to Ref. 39 for the discussion of other topological nodal points for pairing in obstructed TBG bands. As we will show next, band-off-diagonal pairing leads to additional unusual spectral properties with far reaching consequences for graphene moiré systems. To this end, consider the following effective Hamiltonian, $\mathcal{H}_{\sigma_y} = \sum_{\mathbf{k}} c_{\mathbf{k},\alpha,\eta}^\dagger c_{\mathbf{k},\alpha,\eta} \xi_{\eta,\mathbf{k},\alpha} + \sum_{\mathbf{k}} [\Delta_{\mathbf{k}} c_{\mathbf{k},+}^\dagger \sigma_y c_{-\mathbf{k},-}^\dagger + \text{H.c.}]$, where the scalar function $\Delta_{\mathbf{k}}$ describes the form of pairing. We will here study two cases which are conventionally considered to be fully gapped, (i) a momentum-independent “ s -wave state” (A_2 or A pairing in Table I) where $\Delta_{\mathbf{k}} = \Delta_0$ and (ii) a “chiral p -wave” state, or more precisely an $E_2(1, i)$ state, where $\Delta_{\mathbf{k}} = \Delta_0(X_{\mathbf{k}} + iY_{\mathbf{k}})$ with $(X_{\mathbf{k}}, Y_{\mathbf{k}})$ being smooth, MBZ-periodic functions transforming as (x, y) under C_{3z} . Furthermore, we parameterize the dispersion, $\xi_{\eta,\mathbf{k},\alpha}$, of the two flat bands ($\alpha = \pm$) in valley $\eta = \pm$ as $\xi_{\mathbf{k},\alpha} = \epsilon_{\mathbf{k}} - \mu + \alpha \delta_{\mathbf{k}}$, where $\epsilon_{\mathbf{k}}$ and $\delta_{\mathbf{k}}$ are C_{3z} (and, for $D_0 = 0$, C_{2x}) symmetric functions.

The Bogoliubov spectrum of \mathcal{H}_{σ_y} has four bands, given by $\pm \delta_{\mathbf{k}} \pm \sqrt{(\epsilon_{\mathbf{k}} - \mu)^2 + |\Delta_{\mathbf{k}}|^2}$. Consequently, the excitation gap at momentum \mathbf{k} reads as

$$\Delta E_{\mathbf{k}} = \left| |\delta_{\mathbf{k}}| - \sqrt{(\epsilon_{\mathbf{k}} - \mu)^2 + |\Delta_{\mathbf{k}}|^2} \right|, \quad (3)$$

which is shown in Fig. 1(d), and therefore exhibits nodes where $|\delta_{\mathbf{k}}| = \sqrt{(\epsilon_{\mathbf{k}} - \mu)^2 + |\Delta_{\mathbf{k}}|^2}$. As long as the band structure has Dirac points, there are points \mathbf{k}_D in the Brillouin zone with $\delta_{\mathbf{k}_D} = 0$, associated with the blue cross in Fig. 1(d). Furthermore, for a metallic normal state, μ must be within the bandwidth and, hence, there must be a region R in momentum space where $|\delta_{\mathbf{k}}| > |\epsilon_{\mathbf{k}} - \mu|$. For the momentum-independent A_2 state, $\Delta_{\mathbf{k}} = \Delta_0$, this implies that there exists $\Delta_0^>0$ such that there is $\mathbf{k}^* \in R$ with parameters (such as the blue circle) above the red solid line in Fig. 1(d) as long as $|\Delta_0| < \Delta_0^>$. By continuity, this means that there must be a nodal point on any line connecting \mathbf{k}_D and \mathbf{k}^* . Consequently, for μ within the bandwidth and $\delta_{\mathbf{k}_D} = 0$ for some \mathbf{k}_D , the A_2 will always have a nodal line if $|\Delta_0|$ is sufficiently small, consistent with the intuitive picture based on the Bogoliubov spectrum in Fig. 1(a-c).

We illustrate this further in Fig. 1(e) using a toy model with $\delta_{\mathbf{k}} = t|1 + e^{i\mathbf{a}_1 \cdot \mathbf{k}} + e^{-i\mathbf{a}_2 \cdot \mathbf{k}}|$ and $\epsilon_{\mathbf{k}} = t' \sum_{j=1}^3 \cos \mathbf{a}_j \cdot \mathbf{k}$, $\mathbf{a}_j = [C_{3z}]^{j-1}(\sqrt{3}, 0)^T$. This leads to the second unexpected conclusion that, for any pairing mechanism, including conventional electron-phonon coupling, the leading instability either has nodal lines in a finite region below T_c or transforms non-trivially under the symmetries of the normal state. For electron-phonon pairing (or pairing mediated by the fluctuations of any time-reversal-symmetric order parameter [52], such as the T-IVC state) this is particularly unexpected since it is generally believed to always lead to a fully gapped state that transforms trivially under all symmetries. In fact, this can be proven in general terms [51, 52], even for spin-orbit-split Fermi surfaces and beyond mean-field theory [52]. The crucial difference to these works, however, is that spinfull time-reversal is broken in our case such that the Fermi-Dirac constraint is inconsistent with a non-sign-changing, band-diagonal pairing state. This leads to the unique situation that although electron-phonon coupling will lead to entirely attractive interactions in the Cooper channel, the superconducting energetics is frustrated: the dominant pairing state is determined by whether the energetic loss due to non-resonant band-off-diagonal Cooper pairs (A_2 pairing) or the costs from sign changes of the order parameter (such as B_1) are less harmful. We will demonstrate this explicitly by a model calculation in Sec. II E below, where either A_2 or B_1 is dominant, depending on the form of the electron phonon coupling.

Let us first, however, discuss the general spectral properties of the “chiral p -wave” state which is canonically expected to be fully gapped as long as the Fermi surfaces do not cross the zeros of $X_{\mathbf{k}} + iY_{\mathbf{k}}$. Three of these zeros have to be at the Γ , K , and K' points as a consequence of C_{3z} symmetry. In the absence of fine-tuning, $X_{\mathbf{k}} + iY_{\mathbf{k}}$ will have vortices at these points with vorticity $v = +1$. As can be seen in Fig. 1(f), where we show the phase of $X_{\mathbf{k}} + iY_{\mathbf{k}}$ using an admixture of the two lowest-order terms, the net vorticity of $+3$ at these high-symmetry points has to be compensated by anti-vortices at generic momenta. The lowest possible number is three C_{3z} -related vortices, which appear near the M points in Fig. 1(f). If it holds $|\delta_{\mathbf{k}}| > |\epsilon_{\mathbf{k}} - \mu|$ at any of these zeros $\mathbf{k} = \mathbf{k}_j$, we obtain a point above the red line in Fig. 1(d) and, thus, a nodal point along any contour between that \mathbf{k}_j and \mathbf{k}_D ; as opposed to the A_2 state, this holds irrespective of the value of Δ_0 and therefore all the way to zero temperature. In summary, we find that also the $E_2(1, i)$ “chiral p -wave” state is not generically fully gapped but instead will exhibit a nodal line encircling any zero \mathbf{k}_j of $X_{\mathbf{k}} + iY_{\mathbf{k}}$ with $|\delta_{\mathbf{k}_j}| > |\epsilon_{\mathbf{k}_j} - \mu|$. This leads to an interesting filling dependence of the superconducting gap, as we illustrate in our toy model in Fig. 1(g) along with the criterion $D_{\mathbf{k}_j} := |\delta_{\mathbf{k}_j}| - |\epsilon_{\mathbf{k}_j} - \mu| > 0$ evaluated

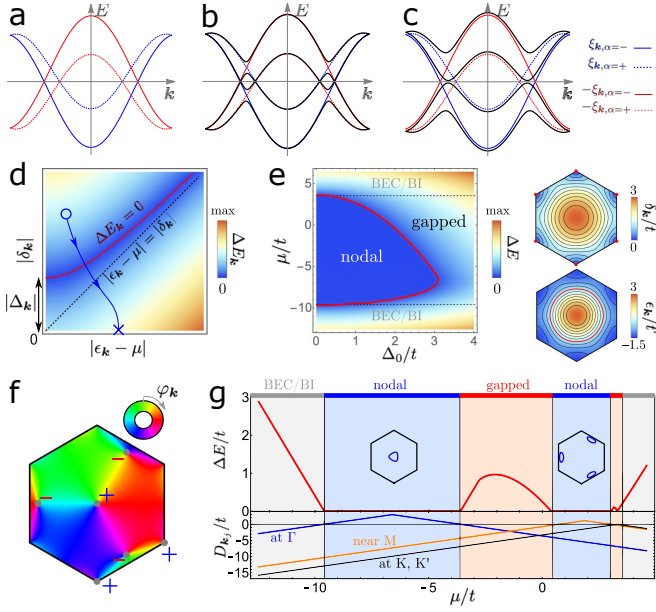


FIG. 1: **Spectral properties of interband pairing.**

While for band-diagonal pairing a small superconducting order parameter can immediately open up a gap as time-reversal symmetry guarantees that the associated avoided crossings [gray regions in (a)] in the Bogoliubov spectrum are at the Fermi level, this is not the case for band-off-diagonal pairing (b). Here, a sufficiently strong order-parameter value is required to establish a full gap, see (c). Its \mathbf{k} dependence according to Eq. (3) is shown in (d), where the red line indicates nodal points. If the band structure has Dirac points, there will be a point on the horizontal axis (blue cross). Consequently, if there is another momentum point located above the red line (blue circle), continuity of the Hamiltonian implies a nodal point on any path connecting the two momenta. (e) Gap of the isotropic A_2 state and $\delta_{\mathbf{k}}$, $\epsilon_{\mathbf{k}}$ (zeros indicated in red) for the normal-state toy model defined in the text. BEC/BI refers to the Bose-Einstein condensate/band insulator limit. (f) Complex phase $\varphi_{\mathbf{k}} = \arg(X_{\mathbf{k}} + iY_{\mathbf{k}})$ for leading basis function with small subleading corrections. (g) Shows the gap of the chiral p -wave $E_2(1, i)$ state with $\Delta_0 = 1.5t$ and the value of $D_{\mathbf{k}_j} := |\delta_{\mathbf{k}_j}| - |\epsilon_{\mathbf{k}_j} - \mu|$ for \mathbf{k}_j at the three symmetry-in-equivalent vortices in (f) as a function of μ . We took $t' = -2.2t$, $t > 0$, in (b,d).

at the vortices at Γ , K/K' , and near M . Depending on μ , $D_{\mathbf{k}}$ is positive only near the Γ point or only in a region surrounding the vortices close to the M points, leading to nodal lines encircling Γ and near the M points, respectively, as shown in the inset of Fig. 1(g). These regimes are separated by a fully gapped region where $D_{\mathbf{k}} < 0$ for all \mathbf{k} , which could explain the fully gapped to nodal transition seen in tunneling experiments [49] when the filling fraction is changed. Note that $D_{\mathbf{k}_j} = -|\epsilon_{\mathbf{k}_j} - \mu| \leq 0$ for \mathbf{k}_j at the K and K' points. In Fig. 1(g), $D_K = D_{K'}$ vanishes close to the top of the band, which simply means that the Fermi surfaces cross the K , K' points and the

superconductor has nodal points for this fine-tuned value of the chemical potential.

C. Fluctuation-induced pairing

Having discussed the unique energetics of pairing and spectral properties of the resulting superconductors in spin-polarized quasi-flat-bands with Dirac cones on a general level, we next study these aspects more explicitly by solving the superconducting self-consistency equations in the flat bands common to alternating-twist graphene systems. We will start with pairing induced by fluctuations of a nearby symmetry-broken phase. To this end, we will couple the low-energy electrons introduced in Eq. (1) to a collective bosonic field $\phi_j(\mathbf{q}) = \phi_j^\dagger(-\mathbf{q})$ via

$$\mathcal{H}_\phi = \sum_{\mathbf{k}, \mathbf{q}, j} c_{\mathbf{k}+\mathbf{q}, \alpha, \eta}^\dagger \lambda_{\alpha, \eta; \alpha', \eta'}^j c_{\mathbf{k}, \alpha', \eta'} \phi_j(\mathbf{q}), \quad (4)$$

where the Hermitian matrices λ^j capture the nature of the correlated insulating phase; we here choose and normalize λ^j such that $(\lambda^j)^2 = \mathbb{1}$. Both for twisted bi-[9] and trilayer graphene [14, 15, 29], the stable phases emerging out of the $U(4) \times U(4)$ [9] manifold in the chiral-flat (decoupled) limit are natural candidates. Integrating out the bosonic modes, we obtain an effective electronic interaction which in the for superconductivity relevant intervalley Cooper channel reads as

$$\mathcal{H}_{\text{int}}^\phi = - \sum_{\mathbf{k}, \mathbf{k}'} \chi_{\mathbf{k}-\mathbf{k}'} \mathcal{V}_{(\eta, \alpha, \beta), (\eta', \alpha', \beta')} \times c_{-\mathbf{k}, \beta, -\eta}^\dagger c_{\mathbf{k}, \alpha, \eta}^\dagger c_{\mathbf{k}', \alpha', \eta'} c_{-\mathbf{k}', \beta', -\eta'}, \quad (5)$$

with vertex

$$\mathcal{V}_{(\eta, \alpha, \beta), (\eta', \alpha', \beta')} = t_\phi \sum_j [\lambda_{\beta, \eta; \beta', \eta'}^j]^* \lambda_{\alpha, \eta; \alpha', \eta'}^j, \quad (6)$$

$t_\phi = \pm 1$ encoding whether the order parameter is even or odd under time-reversal, $\Theta \phi_j(\mathbf{q}) \Theta^\dagger = t_\phi \phi_j(\mathbf{q})$, and $\chi_{\mathbf{q}} > 0$ denoting the (static) susceptibility of ϕ_j .

Before discussing numerical results for the full model, we first focus on perfectly flat bands. In this limit, the leading superconducting instability within mean-field theory is given by the largest eigenvalue of \mathcal{V} in Eq. (6) viewed as a matrix in the multi-index (η, α, β) . Furthermore, if there is an anti-symmetric, valley-off-diagonal matrix D obeying (see Methods)

$$[D\eta_x, \lambda^j]_{-t_\phi} \equiv D\eta_x \lambda^j - t_\phi \lambda^j D\eta_x = 0, \quad (7)$$

the associated leading superconducting order parameter in Eq. (1) is given by $(\Delta_{\mathbf{k}, \eta})_{\alpha, \alpha'} = \delta_{\mathbf{k}} (D\eta_x)_{\alpha, \eta; \alpha', \eta'}$ with $\delta_{\mathbf{k}} > 0$; here η_j denote Pauli matrices in valley space and the precise form of $\delta_{\mathbf{k}}$ is determined by $\chi(\mathbf{q})$.

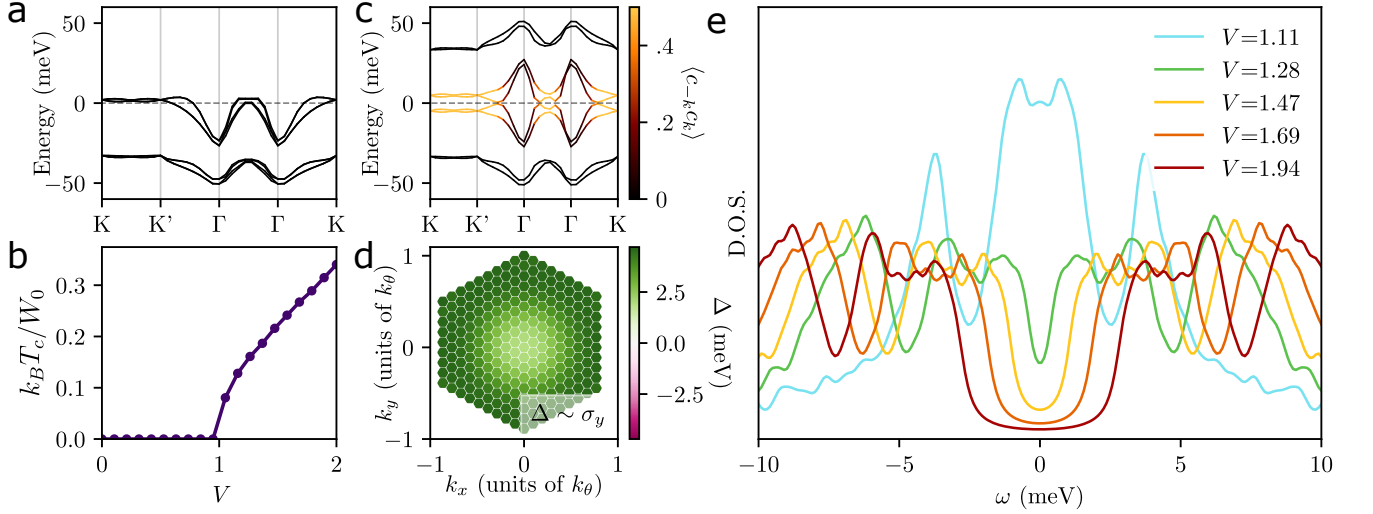


FIG. 2: **Pairing mediated by T-IVC fluctuations.** We show (a) the band structure of the normal state with spin polarization (K, K', and Γ label the high-symmetry points of the moiré scale Brillouin zone) and (b) the critical temperature T_c (in units of the maximum band splitting $W_0 \simeq 9.4$ meV) as a function of coupling strength V measured in units of the critical coupling $V_{c,1} = 105$ meV \cdot nm² obtained from the linearized gap equation. The band structure (with color indicating the band-projected value of the anomalous correlator) of the A_2 state and its order parameter are shown in (c) and (d). The DOS of the $T = 0$ superconductor for several different values of coupling strength V is plotted in (e). The DOS was computed as $\sum_{\mathbf{k}} \delta(E_{\mathbf{k}} - \omega)$, replacing the δ function with Lorentzians with half width at half max 0.3 meV (much smaller than the typical superconducting order parameter). The critical coupling $V_{c,2}$ where the nodal lines disappear is $V_{c,2} \simeq 1.4V_{c,1}$.

D. T-IVC fluctuations

Motivated by recent experiments [7] providing direct evidence for T-IVC order, we start with T-IVC fluctuations as a pairing glue. In the $U(4) \times U(4)$ symmetric limit, the T-IVC state is associated with $\lambda^j = \sigma_0 \eta_j$, $j = x, y$, within our conventions. Since $t_\phi = +1$, we are looking for $D\eta_x$ that commutes with λ^j . Interestingly, there is a unique anti-symmetric, valley-off-diagonal matrix $D \propto \sigma_y \eta_x$ with that property, implying that the leading pairing state has the form $\Delta_{\mathbf{k}, \eta} = \sigma_y \delta_{\mathbf{k}}$, $\delta_{\mathbf{k}} > 0$. This is exactly the A_2 state in Table I, which, as discussed above, will have nodal lines at least in the vicinity of T_c when a finite band dispersion is taken into account. Intuitively, the fact that A_2 pairing is favored can be understood by noticing that the valley-off-diagonal form of λ^j leads to an attractive interaction across the valleys, which penalizes the B_1 state with its sign change between the two valleys. In fact, it holds $\mathcal{V}_{(\eta, \alpha, \beta), (\eta', \alpha', \beta')} = (1 - \eta \eta') \sum_{\mu=0}^3 (\sigma_\mu^*)_{\alpha, \beta} (\sigma_\mu)_{\alpha', \beta'}$ showing explicitly that it is repulsive (attractive) in the B_1 (A_2) channel.

To go beyond the flat-band limit, we solve the superconducting mean-field equations numerically. We take the flat TBG bands from the continuum model [66] as the starting point. To capture the spin polarized normal state, we supplement it with Coulomb repulsion and

a perform HF calculation (see Appendix A for details). As can be seen in the resulting band structure shown in Fig. 2(a) with interaction renormalization assuming filling fraction $\nu = 2$, this not only pushes one spin flavor below the Fermi level but also induces significant band renormalizations. For our subsequent study of superconductivity, we project onto the two bands at the Fermi level and associate them with the creation operators $c_{\mathbf{k}, \alpha}$ in the interactions in Eqs. (4) and (5). In our numerical computations, we choose $\chi(\mathbf{q}) = \frac{1}{A_m} \frac{V}{\alpha^2 + |\mathbf{q}|^2/k_\theta^2}$ where A_m is the real space area of a moiré unit cell, and take $\alpha = 0.05$ for concreteness, although we checked our main conclusion do not crucially depend on this form. In all of our numerics, we work at doping $\nu = 2.5$.

As expected, we indeed find that the A_2 state dominates, both right at the critical temperature T_c , obtained from the linearized gap equation, and at $T = 0$ as we show by iteratively solving the full self-consistency equation (see Appendix C). One crucial effect of the finite dispersion and splitting between the bands is that a finite interaction strength, $V > V_{c,1}$, is required to stabilize the superconducting phase, as can be seen in the plot of T_c in Fig. 2(b). Superconductivity ceases to be a weak-coupling instability as the Bloch states $(\mathbf{k}, \alpha, \eta)$ and $(-\mathbf{k}, \alpha', -\eta)$ are not degenerate for $\alpha \neq \alpha'$, cutting off the logarithmic divergence known from BCS theory. The quasi-particle spectrum and order parameter

of superconductivity from $T = 0$ numerics are shown in Fig. 2(c,d). In accordance with our general discussion above, we observe that the order parameter only has finite components proportional to σ_y , which do not mix with the band-even contributions $\propto \sigma_{0,x,z}$ as a result of C_{2z} symmetry. Furthermore, it does not change sign as a function of \mathbf{k} and, for sufficiently small V but still with $V > V_{c,1}$, the nodal lines in the superconducting spectrum persist all the way to $T = 0$, while the nodal line is gapped out at low $T < T_c$ if $V > V_{c,2}$.

The interaction-strength-dependence of the superconducting gap can be more clearly seen in Fig. 2(e), where we show the DOS for the self-consistent solution at $T = 0$. For large V , the superconductor becomes fully gapped at $T = 0$, leading to a U-shaped DOS. With smaller V , the magnitude of the order parameter decreases and the superconductor eventually exhibits nodal lines, as explained above. In the regime just before these nodal lines appear, there is an increase in the DOS near the Fermi level, roughly when the order parameter and the maximal band splitting are comparable, leading to a V-shaped DOS (green line). The lifetime parameter used to compute the DOS is 0.3 meV; this choice was based on our k -grid spacing. While it is not necessarily small with respect to the tunneling gap (which vanishes at $V_{c,2}$), it is small with respect to $\Delta(\mathbf{k})$ which is of order 5 meV just as the state is becoming fully gapped for our choice of normal state. This behavior of the DOS with interaction strength may offer a natural explanation for the U-shaped tunneling conductance measurements near $\nu = 2$ and V-shaped tunneling conductance measurements near $\nu = 3$ observed in TTG [49]; if we are considering T-IVC fluctuations of the insulator at $\nu = 2$, then it may be reasonable to expect the coupling to these fluctuations could grow weaker as we dope towards $\nu = 3$, in line with the experimentally observed ν dependence.

Note that the regime we call V-shaped here is strictly speaking fully gapped. However, the crucial difference to the BCS state is that the gap is much smaller than the order parameter magnitude as a result of the different Bogoliubov spectrum in Eq. (3). This is why, depending not only on the magnitude of the pairing but also on the precise form of the normal state, the resulting tunneling spectra can resemble those observed experimentally [48, 49], such as the green curve in Fig. 2(e), making the A_2 state an attractive candidate. The regime of small V where stable superconductivity with true Bogoliubov Fermi surfaces is observed can further exhibit a peak at $\omega = 0$ which is due to a Van Hove singularity crossing the Fermi level, see blue curve in Fig. 2(e); while this peak has not been observed experimentally, its presence crucially depends on details of the normal state band structure and is only found to be energetically favored in a very small regime of V in our model.

E. Electron-phonon coupling

To illustrate that the off-diagonal A_2 state is more generally favored beyond just T-IVC fluctuations, we next discuss electron-phonon coupling, which is frequently considered as a plausible pairing mechanism for twisted moiré systems [33, 35–39]. Similar to Ref. 35, we use that the optical A_1 , B_1 , and E_2 phonon modes are known [68] to dominate the electron-phonon coupling in single-layer graphene. As these are optical phonons, we further assume that the impact of the interlayer coupling on the phonons can be neglected and arrive at

$$\mathcal{H}_{EP} = \int d\mathbf{r} \psi_{\ell,s}^\dagger(\mathbf{r}) [g_{A_1} \Lambda_{A_1} u_{A_1,\mu}(\mathbf{r}) + g_{B_1} \Lambda_{B_1} u_{B_1,\mu}(\mathbf{r}) + g_{E_2} \Lambda_{E_2} \cdot \mathbf{u}_{E_2,\mu}(\mathbf{r})] (\mathbf{v}_\mu)_\ell \psi_{\ell,s}(\mathbf{r}) \quad (8)$$

for the electron-phonon coupling, where \mathbf{v}_μ encode the layer structure of the modes (see Methods). Symmetry dictates that the vertices Λ_g are given by $\Lambda_{A_1} = \eta_x \rho_x$, $\Lambda_{B_1} = \eta_y \rho_y$, and $\Lambda_{E_2} = (\eta_z \rho_y, -\rho_x)$ where ρ acts on the microscopic sublattice basis. Integrating out the phonons and projecting to the flat bands, we obtain an effective electron-electron interaction (see Methods)

$$\mathcal{H}_{\text{int}}^C = - \sum_{\mathbf{k}, \mathbf{k}'} V_g [\lambda_{\mathbf{k}, \beta, \eta; \mathbf{k}', \beta', \eta'}^{g, j, \mu}]^* \lambda_{\mathbf{k}, \alpha, \eta; \mathbf{k}', \alpha', \eta'}^{g, j, \mu} \times c_{-\mathbf{k}, \beta, -\eta}^\dagger c_{\mathbf{k}, \alpha, \eta}^\dagger c_{\mathbf{k}', \alpha', \eta'}^C c_{-\mathbf{k}', \beta', -\eta'}^C, \quad (9)$$

where the coupling constants V_g of the three different phonon modes $g = A_1, B_1, E_2$ are estimated to obey $V_{A_1} = V_{B_1} \simeq 1.33 V_{E_2}$ for parallel spins in the two valleys, while $V_{A_1} = V_{B_1} = 0$ for anti-parallel spins. From Eq. (9), it is clear that the induced interaction would be always completely attractive if we focused on intra-band pairing, $\alpha = \alpha' = \beta = \beta'$, which in spinful systems generically favors the trivial pairing channel [51, 52]. In our case, the combination of two energetically close bands and the trivial pairing being purely band-off-diagonal leads to the competition between different superconductors, even with electron-phonon coupling alone.

To demonstrate this, we study intra-valley pairing within the mean-field approximation and parametrize the relative strength of the different phonon modes with an angle variable θ_{ph} according to $V_{A_1} = V_{B_1} = V_0 \cos \theta_{\text{ph}}$, $V_{E_2} = V_0 \sin \theta_{\text{ph}}$. The results of the mean-field calculation are summarized in Fig. 3. We see that the A_2 pairing state is favored by the intervalley phonons ($\theta_{\text{ph}} = 0$) inspite of its band-off-diagonal nature leading to a suppressed gap [see Fig. 3(a)]. This is natural as these phonons mediate an attractive interaction between the two valleys which disfavors the B_1 state, similar to T-IVC fluctuations. In fact, focusing on the leading, momentum independent term, $\lambda_{\mathbf{k}, \mathbf{k}'}^{g, +} \rightarrow \lambda^{g, +}$, $g = A_1, B_1$, symmetry dictates $\lambda^{A_1, +} \propto \sigma_0 \eta_1$ and $\lambda^{B_1, +} \propto \sigma_0 \eta_2$ in

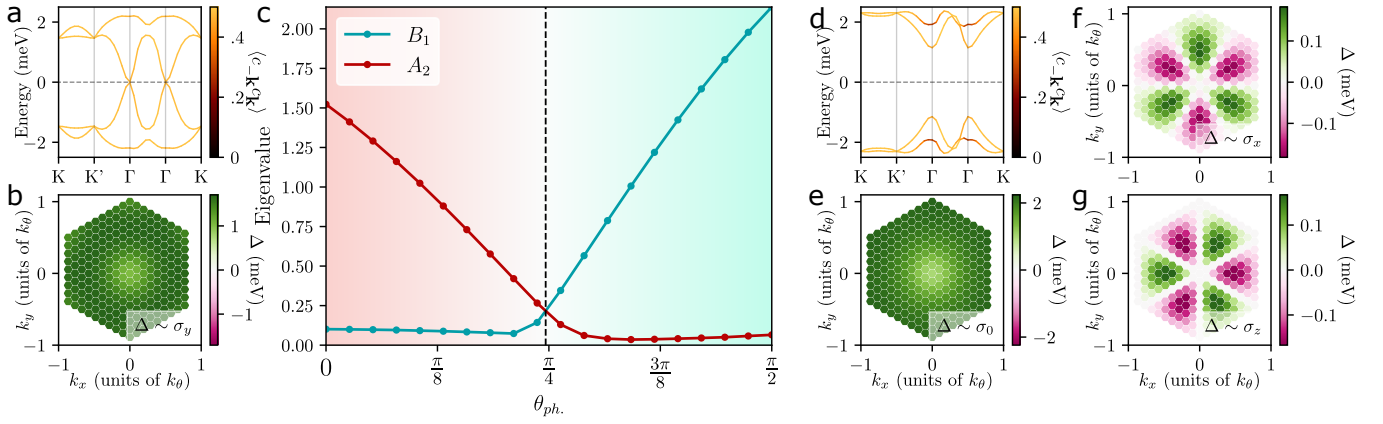


FIG. 3: Pairing from electron-phonon coupling. We show (a) the band structure and (b) the self consistent order parameter of the A_2 pairing for $\theta_{ph} = 0$ and $T = 0$. The eigenvalues corresponding to the A_2 and B_1 pairings in the linearized gap equation at $T = 5$ K, which is close to their T_c , are shown in (c) as a function of θ_{ph} . We show an example of the band structure (d) of the B_1 pairing and its order parameter (e,f,g). In accordance with symmetry, the A_2 (B_1) state only has order-parameter components $\propto \sigma_y$ ($\propto \sigma_{0,x,z}$). We took $\nu = 2.5$ and $V_0 = 250 \text{ meV} \cdot (\text{nm})^2$ with a continuum model bandwidth $\simeq 2 \text{ meV}$. We point out that if A_1 phonons are dominant, as suggested by recent experimental work [61] and past theoretical study in mono-layer graphene [67], we would expect our A_2 pairing to dominate assuming the pairing potential is sufficiently large. We also emphasize that although the pairing functions for A_2 pairing (b) when $\theta = 0$ and B_1 pairing when $\theta = \pi/2$ (e,f,g) are roughly equal, the excitation spectra shows the B_1 state with a band gap on the order of the pairing strength (d) while the A_1 state's band gap is nearly zero, see (a).

the chiral limit (see Appendix D3). This maps the problem exactly to that of T-IVC fluctuations, immediately explaining why the order parameter has a fixed sign in Fig. 3(b). As θ_{ph} is increased, the B_1 state is favored (roughly for $\theta_{ph} > \pi/4$) as can be seen in Fig. 3(c). This is expected since the intervalley E_2 phonon mediates an attractive interaction within each valley such that the energy gain due to the enhanced gap [Fig. 3(d)], associated with the band-diagonal matrix elements of the B_1 state, will overcompensate the energetic loss due to the sign change of B_1 's order parameter between the two valleys. This picture is consistent with the dominance and non-sign-changing nature of the band-diagonal components of the B_1 state, see Fig. 3(e-g). Finally, this behavior can also be understood by applying the commutator criterion in Eq. (7) in the microscopic sublattice basis, see Appendix D1.

This shows that, as opposed to the conventional scenario [51, 52], there are two possible leading superconducting states and the superconducting pairing state does not transform trivially under the symmetries of the system even when phonons alone provide the pairing glue. We have checked in our $T = 0$ numerics that a $60\text{-}70 \text{ meV} \cdot (\text{nm})^2$ coupling to A_1 and B_1 phonons (based on Ref. 68) is roughly of the order needed to stabilize the A_2 pairing, assuming the normal state is the flat bands of the un-renormalized continuum model, which in our case has a bandwidth of 2 meV . However, we note that if the interaction-renormalized band splitting is much larger than the continuum model band width, or if the normal state has anti-parallel spins in either valley, addi-

TABLE II: Leading superconducting states in the flat-band limit, following from Eq. (7), for pairing mediated by fluctuations of the indicated orders, defined by using λ^j in Eq. (4). Here $\delta_{\mathbf{k}} > 0$ and states separated by commas are degenerate. The couplings in the microscopic basis, used in Fig. 4 for the respective orders, are listed under $\bar{\lambda}^j$. Except for SLP−, the leading superconducting states for λ^j and $\bar{\lambda}^j$ are the same (cf. Fig. 4 and Appendix D1).

type	Fluctuating Order		Leading Superconductor	
	λ^j	$\bar{\lambda}^j$	$\Delta_{\mathbf{k},\eta}$	IR
T-IVC	$\sigma_0 \eta_{x,y}$	$\rho_x \eta_{x,y}$	$\sigma_y \delta_{\mathbf{k}}$	A_2
K-IVC	$\sigma_y \eta_{x,y}$	$\rho_y \eta_{x,y}$	$\sigma_0 \eta \delta_{\mathbf{k}}$	B_1
SLP+	$\sigma_y \eta_z$	$\rho_z \eta_0$	$\sigma_y \delta_{\mathbf{k}}, \sigma_0 \eta \delta_{\mathbf{k}}$	A_2, B_1
SLP−	$\sigma_y \eta_0$	$\rho_z \eta_z$	$\sigma_x \eta \delta_{\mathbf{k}}, \sigma_z \eta \delta_{\mathbf{k}}$	B_2, B_1

tional particle-hole fluctuations, such as those of T-IVC order, will also be required for pairing. An interesting scenario arises for anti-parallel spins in the two valley as a magnetic field will cant the spins and, hence, increase the projection of the intervalley phonon matrix elements to the flat bands. At least in TTG, with the suppressed orbital coupling, this could give rise to re-entrant superconductivity at high fields [25].

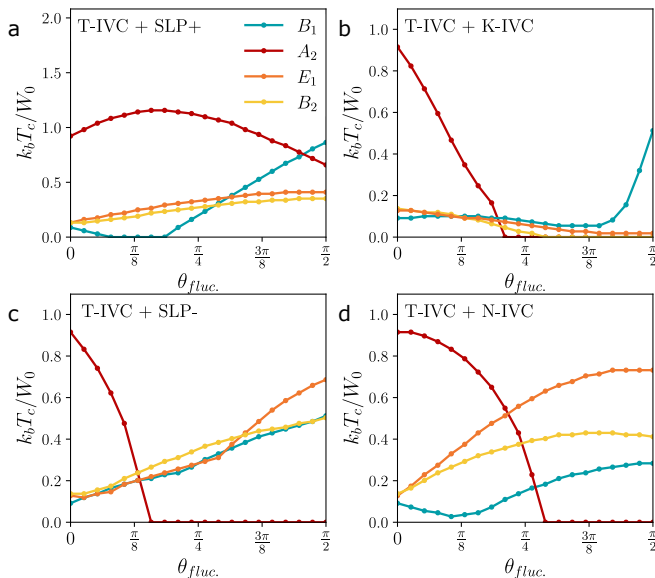


FIG. 4: **Pairing for different particle-hole fluctuations.** These are defined by the coupling matrices $\bar{\lambda}^j$ listed in Table II. Similar to Fig. 3(c), we show T_c of the leading pairing states, where $\theta_{\text{fluc.}}$ tunes the relative strength between T-IVC-induced interactions ($\propto \cos \theta_{\text{fluc.}}$) and interactions ($\propto \sin \theta_{\text{fluc.}}$) coming from fluctuations of (a) SLP+, (b) K-IVC, (c) SLP-, and (d) N-IVC fluctuations.

F. Other particle-hole fluctuations

Finally, we discuss pairing induced by fluctuations of other particle-hole instabilities. In Table II, we list the resulting leading superconductors taking λ^j in Eq. (4) to be any of the different strong-coupling candidate order parameters [9, 13–15, 29]. In particular, in addition to the T-IVC, we will consider the time-reversal-odd Kramers intervalley coherent state (K-IVC), and time reversal-odd and -even sublattice polarized states (SLP- and SLP+). To analyze how sensitive our conclusions are to the precise form of the coupling of the strong-coupling fluctuating orders to the electrons, we also perform numerics by projecting momentum-independent coupling vertices in the microscopic basis with the correct symmetries (see, e.g., Table II in [13]), listed as $\bar{\lambda}^j$ in Table II, to the flat bands. In the band basis, this leads to momentum-dependent coupling vertices, cf. Eq. (9). Motivated by recent experiments [7], we will also consider fluctuations of an additional nematic, time-reversal symmetric, layer-odd, intervalley coherent state (N-IVC) [62] which is not a candidate ground state in the strong coupling limit; unlike the other strong-coupling ground states, the N-IVC has no momentum independent representation in the flat band basis but does have a momentum-independent matrix order parameter in the sublattice basis which takes the form $\lambda^{(j,j')} = (\eta_x, \eta_y)_j (\rho_0, \rho_z)_{j'}$. The results for fluctuations of the projected strong-coupling orders $\bar{\lambda}^j$

in Table II are shown in Fig. 4, where we use the angle $\theta_{\text{fluc.}}$ to tune the relative strength between T-IVC and any of the other type of fluctuation-induced interactions by multiplying the T-IVC interaction potential with $\cos(\theta_{\text{fluc.}})$ and the other fluctuation potential with $\sin(\theta_{\text{fluc.}})$. In our microscopic numerics, we have taken a potential form $\chi(\mathbf{q}) = \frac{1}{A_m} \frac{V}{\alpha^2 + |\mathbf{q}|^2/k_\theta^2}$ again with $\alpha = 0.2$ and with $V = 4200 \text{ meV} \cdot (\text{nm})^2$. We chose the value of V such that the transitions between the different pairing states are clearly visible in Fig. 4 when varying $\theta_{\text{fluc.}}$. In accordance with the prediction for $\bar{\lambda}^j$ in Table II, SLP+ fluctuations further stabilize the A_2 superconductor, see Fig. 4(a). As such, the band-diagonal B_1 superconducting channel, where SLP+ fluctuations are also attractive, can become the leading channel (favored over A_2 as a result of the finite bandwidth) only very close to $\theta_{\text{fluc.}} = \pi/2$. K-IVC fluctuations, however, are repulsive for A_2 pairing and favor the B_1 state more strongly.

So far, the strong-coupling (λ^j) and sublattice ($\bar{\lambda}^j$) form of the couplings in Table II lead to the same conclusions. This is different for SLP- fluctuations [Fig. 4(d)], where the projection-induced momentum-dependence in the band basis can stabilize the E_1 superconductor. This can be understood by applying Eq. (7) in the sublattice basis (see Appendix D1). We also find the E_1 state when fluctuations of the N-IVC state of Ref. 62 dominate. Examples of the E_1 nematic and B_2 order parameters which emerge for SLP- fluctuations or N-IVC fluctuations are shown in Appendix F. We point out the nematic E_1 pairing is also an interesting candidate given that despite having nonzero pairing in the $\sigma_0, \sigma_x, \sigma_z$ channels, it will be nodal as long as the σ_x components do not gap out the nodes in the band-diagonal parts.

III. DISCUSSION

Taken together, we see that the proposed band-off-diagonal A_2 superconductor is an especially attractive candidate for TBG and TTB: first, it can lead to both V-shaped or U-shaped DOS, depending on lifetime parameters, the normal state, and the coupling strength V , see Fig. 2(e). As these parameters might vary from sample to sample and within a sample (e.g., V is expected to decrease upon doping further away from the insulator), this can naturally explain the tunneling data of [48, 49]. We emphasize however that at least at the level of our mean-field numerics, we only expect a V-shape in the regime where the superconducting pairing is of the order of the bandwidth; this is the regime, where although the pairing is finite and can be quite large, the gap in the superconducting spectrum is either just closing or very small relative to the pairing. Increasing the pairing further will lead to an evolution from V to U shaped while decreasing the pairing will eventually lead

to a nodal Fermi surface and presumably a peak at zero energy in the DOS. Second, despite its interband nature, A_2 is the unique pairing state that is favored by fluctuations of two out of the four strong-coupling-candidates we consider for the correlated insulator, see Fig. 4(a-c). What is more, this includes the T-IVC state, signatures of which are observed in recent experiments [7]. Finally, it is also favored by the likely dominant [61, 67] optical intervalley phonon modes. We emphasize that, both in the case of fluctuating correlated insulators and phonons, the minimum attractive coupling needed to stabilize a purely band off diagonal state depends on the energy splitting between the two flat bands in the normal state; if the bands of our normal state are closer to degenerate, irrespective of the total bandwidth, the needed coupling to stabilize the A_2 pairing in mean-field will decrease.

The other band-off-diagonal superconductor we identify transforms under the IR E_2 , i.e., can be thought of as a p -wave state. Its spectral properties also agree well with experiment as the chiral configurations, $E_2(1, i)$, which is favored within mean-field theory over a nematic E_2 state, can also have nodal regions, depending on filling. As can be seen in Fig. 1(g), this can lead to a transition from gapped to nodal when increasing the electron filling starting at $\nu \simeq 2$. However, as opposed to the A_2 state, E_2 does not naturally appear as leading instability when considering optical phonons or fluctuations of any of the strong-coupling order parameters of the correlated insulator. While this makes it energetically less natural than A_2 , we cannot exclude it since its phenomenology agrees well with experiment and since the precise form of the coupling of the dominant low-energy collective excitations are not known—significant momentum dependencies beyond λ^j and $\bar{\lambda}^j$ in Table II could stabilize E_2 pairing as well. We also find in our numerics a nematic E_1 state which may be preferred over its chiral version in the presence of sufficient strain or due to fluctuation corrections [27, 53–55]. We find the E_1 state is the leading instability of nematic IVC fluctuations and SLP—fluctuations, and is a subleading instability of T-IVC fluctuations. The E_1 state is interesting in its own right, as it can also be nodal.

As superconductivity might further coexist with T-IVC order [7], we have checked (see Appendix E) that this does not alter our main observation: the preserved C_{2z} symmetry still allows for entirely band-off-diagonal states, with transitions from nodal to full gapped, which are stabilized (among other fluctuations) by intervalley phonons.

For the future, it will be interesting to go beyond mean-field and analyze the competition of our band-off-diagonal states with odd-frequency pairing, which we study in a follow-up work [69]. It also seems promising to study Andreev reflection [48, 49] for our interband pairing scenario. On a more general level, our work shows

that the observation of nodal pairing in twisted graphene systems does not immediately exclude a chiral superconducting state nor an entirely electron-phonon-based pairing mechanism. It illustrates that a microscopic understanding of the superconducting states in graphene moiré systems requires taking into account their intrinsically multi-band nature.

Note added. Just before posting our work, Ref. 70 appeared online, which discusses pairing induced by A_1 phonons in spinful TBG bands.

Methods

Flat-band limit. To derive Eq. (7), we take the flat-band limit, $\xi_{\mathbf{k},\pm} \rightarrow 0$, in the linearized gap equation. For the interaction defined in Eqs. (4-6), we get (with moiré cell area A_m)

$$(\Delta_{\mathbf{k},\eta})_{\beta,\beta'} = t_\phi \frac{1}{4A_m T} \sum_{\mathbf{k}'} \chi_{\mathbf{k}-\mathbf{k}'} \times \sum_j [\lambda_{\beta',\eta;\alpha',\eta'}^j]^* \lambda_{\beta,\eta;\alpha,\eta'}^j (\Delta_{\mathbf{k}',\eta'})_{\alpha,\alpha'}. \quad (10)$$

We define $(\hat{\Delta}_{\mathbf{k}})_{\alpha,\eta;\alpha',\eta'} := (\Delta_{\mathbf{k},\eta})_{\alpha,\alpha'} \delta_{\eta,\eta'}$ and note that finding the leading superconducting state according to Eq. (10) is equivalent to determining $\hat{\Delta}_{\mathbf{k}}$ that maximizes the functional

$$\mathcal{F}[\hat{\Delta}_{\mathbf{k}}] := \frac{\sum_{\mathbf{k},\mathbf{k}',j} \chi_{\mathbf{k}-\mathbf{k}'} t_\phi \text{tr}[\lambda^j \hat{\Delta}_{\mathbf{k}'} (\lambda^j)^\dagger \hat{\Delta}_{\mathbf{k}}^\dagger]}{\sum_{\mathbf{k}} \text{tr}[\hat{\Delta}_{\mathbf{k}}^\dagger \hat{\Delta}_{\mathbf{k}}]}. \quad (11)$$

Since $\chi_{\mathbf{k}-\mathbf{k}'} > 0$, the maximum value will be reached if we can maximize $t_\phi \text{tr}[\lambda^j \hat{\Delta}_{\mathbf{k}'} (\lambda^j)^\dagger \hat{\Delta}_{\mathbf{k}}^\dagger]$ for each $\mathbf{k}, \mathbf{k}', j$ separately. As the Frobenius inner product $\langle A, B \rangle_F = \text{tr}[A^\dagger B]$ reaches its maximum (minimum) at fixed $\langle A, A \rangle$ and $\langle B, B \rangle$, if $A = cB$ with $c > 0$ ($c < 0$), $t_\phi \text{tr}[\lambda^j \hat{\Delta}_{\mathbf{k}'} (\lambda^j)^\dagger \hat{\Delta}_{\mathbf{k}}^\dagger]$ is maximized if $\hat{\Delta}_{\mathbf{k}} = t_\phi c_{\mathbf{k},\mathbf{k}'} \lambda^j \hat{\Delta}_{\mathbf{k}'} (\lambda^j)^\dagger$ with $c_{\mathbf{k},\mathbf{k}'} > 0$. For the ansatz $\hat{\Delta}_{\mathbf{k}} = \delta_{\mathbf{k}} D\eta_x$ (and assuming for now that $\delta_{\mathbf{k}}$ has a fixed sign for all \mathbf{k}), this is obeyed if

$$D\eta_x = t_\phi \lambda^j D\eta_x (\lambda^j)^\dagger, \quad \forall j. \quad (12)$$

We state Eq. (12) as the (anti)commutator condition (7) in the main text [equivalent if $(\lambda^j)^2 = \mathbb{1}$], not only because it highlights the simple algebraic and basis independent nature of the condition but also since it emphasizes the similarities to the generalized Anderson theorem of [71, 72].

If we can find a solution to Eq. (12), we know that the maximum (or at least one of the possibly degenerate maxima) of $\mathcal{F}[\hat{\Delta}_{\mathbf{k}}]$ is of the form of $\hat{\Delta}_{\mathbf{k}} = \delta_{\mathbf{k}} D\eta_x$ where $\delta_{\mathbf{k}}$ is obtained as the maximum of the reduced functional

$$\tilde{\mathcal{F}}[\delta_{\mathbf{k}}] := \frac{\sum_{\mathbf{k},\mathbf{k}'} \chi_{\mathbf{k}-\mathbf{k}'} \delta_{\mathbf{k}}^* \delta_{\mathbf{k}'}}{\sum_{\mathbf{k}} |\delta_{\mathbf{k}}|^2}, \quad (13)$$

or equivalently as the largest eigenvector of $\chi_{\mathbf{k}-\mathbf{k}'}$ viewed as a matrix in \mathbf{k} and \mathbf{k}' . As $\chi_{\mathbf{k}-\mathbf{k}'} > 0$ (due to stability), the Perron-Frobenius theorem then immediately implies $\delta_{\mathbf{k}} > 0$, in line with our assumption above and as stated in the main text.

Electron-phonon coupling. To present more details on the electron-phonon coupling, the associated displacement operators in Eq. (8) can be expressed in terms of canonical bosons, $b_{g,\alpha,\mu,\mathbf{q}}$,

$$(u_{g,\mu}(\mathbf{r}))_j = \sum_{\mathbf{q}} \frac{b_{g,j,\mu,\mathbf{q}} e^{i\mathbf{q}\cdot\mathbf{r}} + \text{H.c.}}{\sqrt{2NM\omega_g(\mathbf{q})}}, \quad (14)$$

where j refers to the two components for the E_2 phonon (is idle for A_1, B_1), M is the carbon mass, and $\omega_g(\mathbf{q})$ is the phonon dispersion, characterizing the phononic part of the Hamiltonian, $\mathcal{H}_P = \sum_{\mathbf{q}} \omega_g(\mathbf{q}) b_{g,j,\mu,\mathbf{q}}^\dagger b_{g,j,\mu,\mathbf{q}}$.

As for $(v_\mu)_\ell$ in Eq. (8), $\ell = 1, 2$ refers to the physical graphene layer in the case of TBG. One can, in principle, choose any orthonormal basis; we will find it convenient to use the layer-exchange even and odd states, $\mathbf{v}_\pm = (1, \pm 1)^T / \sqrt{2}$. For TTG, the situation is more involved (see Appendix D2), but our arguments about which phonons are attractive in which pairing channels will hold for both systems.

We project \mathcal{H}_{EP} in Eq. (8) onto the two flat bands ($\alpha = \pm$) in each valley η of the spin polarized continuum-model, leading to a coupling term similar to Eq. (4) with momentum-dependent coupling matrices, $\lambda^j \rightarrow \lambda_{\mathbf{k},\mathbf{k}'}^{g,j,\mu}$. Investigating the matrix elements $\lambda_{\mathbf{k},\mathbf{k}'}^{g,j,\mu}$, we notice that they almost vanish for the layer-odd intervalley (A_1, B_1) phonons, which can be understood as a consequence of chiral and particle-hole symmetry (see Appendix D3). The situation is the reverse for the intravalley (E_2) phonons, where the layer-even matrix elements are numerically small and the layer-odd matrix elements dominate. We therefore focus on layer-even (odd) intervalley (intravalley) phonon couplings.

Neglecting the momentum dependence in the phonon frequencies and retardation effects, the resulting electron-electron interaction in the inter-valley Cooper channel obtained by integrating out the phonons is given by Eq. (9). Here, $V_g = g_g^2 / (2N\omega_g^2) > 0$ and $V_{A_1} = V_{B_1} \simeq 1.33V_{E_2}$ results from $g_{A_1} = g_{B_1} \simeq g_{E_2}$ and the phonon frequencies estimated in Ref. 68. Importantly, this only

holds for parallel spins in the two valleys. For anti-parallel spins, the projection of the coupling matrices to the flat bands vanishes for the intervalley phonon modes A_1 and B_1 such that $V_{A_1} = V_{B_1} = 0$.

DATA AVAILABILITY

The data generated in this study are available in the Zenodo database under the accession code <https://zenodo.org/record/8381555> and in the figshare repository <https://doi.org/10.6084/m9.figshare.23897019>.

CODE AVAILABILITY

The codes used to generate the plots are available from the corresponding author on request.

ACKNOWLEDGMENTS

M.S.S. acknowledges funding by the European Union (ERC-2021-STG, Project 101040651—SuperCorr). Views and opinions expressed are however those of the authors only and do not necessarily reflect those of the European Union or the European Research Council Executive Agency. Neither the European Union nor the granting authority can be held responsible for them. M.C. and S.S. acknowledge funding by U.S. National Science Foundation grant No. DMR-2002850. M.S.S. thanks B. Putzer for discussions. M.C. thanks P. Ledwith and J. Dong, and D. Parker for helpful discussions.

AUTHOR CONTRIBUTIONS STATEMENT

M.C., S.S., and M.S.S. contributed to the research. M.C. and M.S.S. performed the numerical computations and wrote the paper.

COMPETING INTERESTS STATEMENT

The authors declare no competing interests.

-
- [1] E. Y. Andrei and A. H. MacDonald, “Graphene bilayers with a twist,” *Nature Materials* **19**, 1265 (2020).
 [2] L. Balents, C. R. Dean, D. K. Efetov, and A. F. Young, “Superconductivity and strong correlations in moiré flat bands,” *Nature Physics* **16**, 725 (2020).

- [3] Y. Cao, V. Fatemi, A. Demir, S. Fang, S. L. Tomarken, J. Y. Luo, J. D. Sanchez-Yamagishi, K. Watanabe, T. Taniguchi, E. Kaxiras, R. C. Ashoori, and P. Jarillo-Herrero, “Correlated insulator behaviour at half-filling in magic-angle graphene superlattices,” *Nature* **556**, 80

- (2018).
- [4] X. Lu, P. Stepanov, W. Yang, M. Xie, M. A. Aamir, I. Das, C. Urgell, K. Watanabe, T. Taniguchi, G. Zhang, A. Bachtold, A. H. MacDonald, and D. K. Efetov, “Superconductors, orbital magnets and correlated states in magic-angle bilayer graphene,” *Nature* **574**, 653 (2019).
 - [5] A. L. Sharpe, E. J. Fox, A. W. Barnard, J. Finney, K. Watanabe, T. Taniguchi, M. A. Kastner, and D. Goldhaber-Gordon, “Emergent ferromagnetism near three-quarters filling in twisted bilayer graphene,” *Science* **365**, 605 (2019).
 - [6] K. P. Nuckolls, M. Oh, D. Wong, B. Lian, K. Watanabe, T. Taniguchi, B. A. Bernevig, and A. Yazdani, “Strongly correlated chern insulators in magic-angle twisted bilayer graphene,” *Nature* **588**, 610 (2020).
 - [7] K. P. Nuckolls, R. L. Lee, M. Oh, D. Wong, T. Soejima, J. P. Hong, D. Călugăru, J. Herzog-Arbeitman, B. A. Bernevig, K. Watanabe, T. Taniguchi, N. Regnault, M. P. Zaletel, and A. Yazdani, “Quantum textures of the many-body wavefunctions in magic-angle graphene,” (2023).
 - [8] J. Kang and O. Vafek, “Strong Coupling Phases of Partially Filled Twisted Bilayer Graphene Narrow Bands,” *Phys. Rev. Lett.* **122**, 246401 (2019), [arXiv:1810.08642 \[cond-mat.str-el\]](#).
 - [9] N. Bultinck, E. Khalaf, S. Liu, S. Chatterjee, A. Vishwanath, and M. P. Zaletel, “Ground State and Hidden Symmetry of Magic-Angle Graphene at Even Integer Filling,” *Phys. Rev. X* **10**, 031034 (2020), [arXiv:1911.02045 \[cond-mat.str-el\]](#).
 - [10] T. Soejima, D. E. Parker, N. Bultinck, J. Hauschild, and M. P. Zaletel, “Efficient simulation of moiré materials using the density matrix renormalization group,” *Phys. Rev. B* **102** (2020).
 - [11] F. Xie, A. Cowsik, Z.-D. Song, B. Lian, B. A. Bernevig, and N. Regnault, “Twisted bilayer graphene. VI. an exact diagonalization study at nonzero integer filling,” *Phys. Rev. B* **103** (2021), [10.1103/physrevb.103.205416](#).
 - [12] Y. Kwan, G. Wagner, T. Soejima, M. Zaletel, S. Simon, S. Parameswaran, and N. Bultinck, “Kekulé spiral order at all nonzero integer fillings in twisted bilayer graphene,” *Phys. Rev. X* **11** (2021), [10.1103/physrevx.11.041063](#).
 - [13] M. Christos, S. Sachdev, and M. S. Scheurer, “Correlated Insulators, Semimetals, and Superconductivity in Twisted Trilayer Graphene,” *Phys. Rev. X* **12**, 021018 (2022), [arXiv:2106.02063 \[cond-mat.str-el\]](#).
 - [14] F. Xie, N. Regnault, D. Călugăru, B. A. Bernevig, and B. Lian, “Twisted symmetric trilayer graphene. II. projected hartree-fock study,” *Phys. Rev. B* **104** (2021), [10.1103/physrevb.104.115167](#).
 - [15] P. J. Ledwith, E. Khalaf, Z. Zhu, S. Carr, E. Kaxiras, and A. Vishwanath, “Tb or not tb? contrasting properties of twisted bilayer graphene and the alternating twist n -layer structures ($n = 3, 4, 5, \dots$),” (2021), [arXiv:2111.11060 \[cond-mat.str-el\]](#).
 - [16] G. Wagner, Y. H. Kwan, N. Bultinck, S. H. Simon, and S. Parameswaran, “Global phase diagram of the normal state of twisted bilayer graphene,” *Phys. Rev. Lett.* **128** (2022), [10.1103/physrevlett.128.156401](#).
 - [17] T. Wang, D. E. Parker, T. Soejima, J. Hauschild, S. Anand, N. Bultinck, and M. P. Zaletel, “Kekulé spiral order in magic-angle graphene: a density matrix renormalization group study,” (2022), [arXiv:2211.02693 \[cond-mat.str-el\]](#).
 - [18] Y. H. Kwan, G. Wagner, N. Bultinck, S. H. Simon, E. Berg, and S. A. Parameswaran, “Electron-phonon coupling and competing kekulé orders in twisted bilayer graphene,” (2023), [arXiv:2303.13602 \[cond-mat.str-el\]](#).
 - [19] D. Wong, K. P. Nuckolls, M. Oh, B. Lian, Y. Xie, S. Jeon, K. Watanabe, T. Taniguchi, B. A. Bernevig, and A. Yazdani, “Cascade of electronic transitions in magic-angle twisted bilayer graphene,” *Nature* **582**, 198 (2020).
 - [20] U. Zondiner, A. Rozen, D. Rodan-Legrain, Y. Cao, R. Queiroz, T. Taniguchi, K. Watanabe, Y. Oreg, F. von Oppen, A. Stern, E. Berg, P. Jarillo-Herrero, and S. Ilani, “Cascade of phase transitions and dirac revivals in magic-angle graphene,” *Nature* **582**, 203 (2020).
 - [21] J. M. Park, Y. Cao, K. Watanabe, T. Taniguchi, and P. Jarillo-Herrero, “Tunable strongly coupled superconductivity in magic-angle twisted trilayer graphene,” *Nature* **590**, 249 (2021).
 - [22] Z. Hao, A. M. Zimmerman, P. Ledwith, E. Khalaf, D. H. Najafabadi, K. Watanabe, T. Taniguchi, A. Vishwanath, and P. Kim, “Electric field-tunable superconductivity in alternating-twist magic-angle trilayer graphene,” *Science* **371**, 1133 (2021).
 - [23] J.-X. Lin, P. Siriviboon, H. D. Scammell, S. Liu, D. Rhodes, K. Watanabe, T. Taniguchi, J. Hone, M. S. Scheurer, and J. I. A. Li, “Zero-field superconducting diode effect in small-twist-angle trilayer graphene,” *Nature Physics* **18**, 1221 (2022).
 - [24] E. Morissette, J.-X. Lin, D. Sun, L. Zhang, S. Liu, D. Rhodes, K. Watanabe, T. Taniguchi, J. Hone, J. Pollanen, M. S. Scheurer, M. Lilly, A. Mounce, and J. I. A. Li, “Dirac revivals drive a resonance response in twisted bilayer graphene,” *Nature Physics* (2023), [10.1038/s41567-023-02060-0](#).
 - [25] Y. Cao, J. M. Park, K. Watanabe, T. Taniguchi, and P. Jarillo-Herrero, “Pauli-limit violation and re-entrant superconductivity in moirégraphene,” *Nature* **595**, 526 (2021).
 - [26] R. Ojajärvi, T. Hyart, M. A. Silaev, and T. T. Heikkilä, “Competition of electron-phonon mediated superconductivity and stoner magnetism on a flat band,” *Phys. Rev. B* **98**, 054515 (2018).
 - [27] M. S. Scheurer and R. Samajdar, “Pairing in graphene-based moiré superlattices,” *Phys. Rev. Research* **2**, 033062 (2020).
 - [28] E. Lake, A. S. Patri, and T. Senthil, “Pairing symmetry of twisted bilayer graphene: A phenomenological synthesis,” *Phys. Rev. B* **106** (2022), [10.1103/physrevb.106.104506](#).
 - [29] M. Christos, S. Sachdev, and M. S. Scheurer, “Superconductivity, correlated insulators, and Wess-Zumino-Witten terms in twisted bilayer graphene,” *Proceedings of the National Academy of Science* **117**, 29543 (2020), the T-IVC state was denoted IVC+ in this paper, [arXiv:2007.00007 \[cond-mat.str-el\]](#).
 - [30] E. Khalaf, S. Chatterjee, N. Bultinck, M. P. Zaletel, and A. Vishwanath, “Charged skyrmions and topological origin of superconductivity in magic-angle graphene,” *Science Advances* **7** (2021), [10.1126/sciadv.abf5299](#).

- [31] E. Khalaf, P. Ledwith, and A. Vishwanath, “Symmetry constraints on superconductivity in twisted bilayer graphene: Fractional vortices, $4e$ condensates, or nonunitary pairing,” *Phys. Rev. B* **105**, 224508 (2022).
- [32] H. D. Scammell, J. I. A. Li, and M. S. Scheurer, “Theory of zero-field superconducting diode effect in twisted trilayer graphene,” *2D Materials* **9**, 025027 (2022).
- [33] G. Shavit, E. Berg, A. Stern, and Y. Oreg, “Theory of correlated insulators and superconductivity in twisted bilayer graphene,” *Phys. Rev. Lett.* **127**, 247703 (2021).
- [34] V. Crépel, T. Cea, L. Fu, and F. Guinea, “Unconventional superconductivity due to interband polarization,” *Phys. Rev. B* **105**, 094506 (2022).
- [35] F. Wu, A. H. MacDonald, and I. Martin, “Theory of phonon-mediated superconductivity in twisted bilayer graphene,” *Phys. Rev. Lett.* **121**, 257001 (2018).
- [36] B. Lian, Z. Wang, and B. A. Bernevig, “Twisted bilayer graphene: A phonon-driven superconductor,” *Phys. Rev. Lett.* **122**, 257002 (2019).
- [37] C. Lewandowski, D. Chowdhury, and J. Ruhman, “Pairing in magic-angle twisted bilayer graphene: Role of phonon and plasmon umklapp,” *Phys. Rev. B* **103**, 235401 (2021).
- [38] C. Lewandowski, S. Nadj-Perge, and D. Chowdhury, “Does filling-dependent band renormalization aid pairing in twisted bilayer graphene?” *npj Quantum Materials* **6**, 82 (2021).
- [39] J. Yu, M. Xie, F. Wu, and S. Das Sarma, “Euler Obstructed Cooper Pairing in Twisted Bilayer Graphene: Nematic Nodal Superconductivity and Bounded Superfluid Weight,” *arXiv e-prints* (2022), 10.48550/arXiv.2202.02353, [arXiv:2202.02353 \[cond-mat.supr-con\]](#).
- [40] V. o. T. Phong, P. A. Pantaleón, T. Cea, and F. Guinea, “Band structure and superconductivity in twisted trilayer graphene,” *Phys. Rev. B* **104**, L121116 (2021).
- [41] Y. Wang, J. Kang, and R. M. Fernandes, “Topological and nematic superconductivity mediated by ferro-SU(4) fluctuations in twisted bilayer graphene,” *Phys. Rev. B* **103** (2021), 10.1103/physrevb.103.024506.
- [42] C. Huang, N. Wei, W. Qin, and A. H. MacDonald, “Pseudospin paramagnons and the superconducting dome in magic angle twisted bilayer graphene,” *Phys. Rev. Lett.* **129**, 187001 (2022).
- [43] A. Fischer, L. Klebl, C. Honerkamp, and D. M. Kennes, “Spin-fluctuation-induced pairing in twisted bilayer graphene,” *Phys. Rev. B* **103**, L041103 (2021).
- [44] J. Herzog-Arbeitman, A. Chew, K.-E. Huhtinen, P. Törmä, and B. A. Bernevig, “Many-Body Superconductivity in Topological Flat Bands,” *arXiv e-prints* (2022), [arXiv:2209.00007 \[cond-mat.str-el\]](#).
- [45] T. Cea and F. Guinea, “Coulomb interaction, phonons, and superconductivity in twisted bilayer graphene,” *Proceedings of the National Academy of Sciences* **118** (2021), 10.1073/pnas.2107874118.
- [46] V. Kozii, M. P. Zaletel, and N. Bultinck, “Spin-triplet superconductivity from intervalley goldstone modes in magic-angle graphene,” *Phys. Rev. B* **106** (2022), 10.1103/physrevb.106.235157.
- [47] Y.-Z. You and A. Vishwanath, “Superconductivity from valley fluctuations and approximate $so(4)$ symmetry in a weak coupling theory of twisted bilayer graphene,” *npj Quantum Materials* **4**, 16 (2019).
- [48] M. Oh, K. P. Nuckolls, D. Wong, R. L. Lee, X. Liu, K. Watanabe, T. Taniguchi, and A. Yazdani, “Evidence for unconventional superconductivity in twisted bilayer graphene,” *Nature* **600**, 240 (2021).
- [49] H. Kim, Y. Choi, C. Lewandowski, A. Thomson, Y. Zhang, R. Polski, K. Watanabe, T. Taniguchi, J. Alicea, and S. Nadj-Perge, “Evidence for unconventional superconductivity in twisted trilayer graphene,” *Nature* **606**, 494 (2022).
- [50] P. P. Poduval and M. S. Scheurer, “Vestigial singlet pairing in a fluctuating magnetic triplet superconductor: Applications to graphene moiré systems,” *arXiv e-prints* (2023), [arXiv:2301.01344 \[cond-mat.supr-con\]](#).
- [51] P. M. R. Brydon, S. Das Sarma, H.-Y. Hui, and J. D. Sau, “Odd-parity superconductivity from phonon-mediated pairing: Application to $Cu_xBi_2Se_3$,” *Phys. Rev. B* **90**, 184512 (2014).
- [52] M. S. Scheurer, “Mechanism, time-reversal symmetry, and topology of superconductivity in noncentrosymmetric systems,” *Phys. Rev. B* **93**, 174509 (2016).
- [53] P. W. Anderson and W. F. Brinkman, “Anisotropic superfluidity in 3He : A possible interpretation of its stability as a spin-fluctuation effect,” *Phys. Rev. Lett.* **30**, 1108 (1973).
- [54] V. Kozii, H. Isobe, J. W. F. Venderbos, and L. Fu, “Nematic superconductivity stabilized by density wave fluctuations: Possible application to twisted bilayer graphene,” *Phys. Rev. B* **99**, 144507 (2019).
- [55] V. Gali and R. M. Fernandes, “Role of electromagnetic gauge-field fluctuations in the selection between chiral and nematic superconductivity,” *Phys. Rev. B* **106**, 094509 (2022).
- [56] P. M. R. Brydon, D. F. Agterberg, H. Menke, and C. Timm, “Bogoliubov Fermi surfaces: General theory, magnetic order, and topology,” *Phys. Rev. B* **98** (2018).
- [57] D. Agterberg, P. Brydon, and C. Timm, “Bogoliubov Fermi Surfaces in Superconductors with Broken Time-Reversal Symmetry,” *Phys. Rev. Lett.* **118** (2017).
- [58] N. Read and S. Sachdev, “Spin-Peierls, valence-bond solid, and Néel ground states of low-dimensional quantum antiferromagnets,” *Phys. Rev. B* **42**, 4568 (1990), Appendix B.
- [59] J. Lee and S. Sachdev, “Wess-Zumino-Witten Terms in Graphene Landau Levels,” *Phys. Rev. Lett.* **114**, 226801 (2015), [arXiv:1411.5684 \[cond-mat.str-el\]](#).
- [60] X. Liu, G. Farahi, C.-L. Chiu, Z. Papic, K. Watanabe, T. Taniguchi, M. P. Zaletel, and A. Yazdani, “Visualizing broken symmetry and topological defects in a quantum Hall ferromagnet,” *Science* **375**, 321 (2022), [arXiv:2109.11555 \[cond-mat.mes-hall\]](#).
- [61] C. Chen, K. P. Nuckolls, S. Ding, W. Miao, D. Wong, M. Oh, R. L. Lee, S. He, C. Peng, D. Pei, Y. Li, S. Zhang, J. Liu, Z. Liu, C. Jozwiak, A. Bostwick, E. Rotenberg, C. Li, X. Han, D. Pan, X. Dai, C. Liu, B. A. Bernevig, Y. Wang, A. Yazdani, and Y. Chen, “Strong inter-valley electron-phonon coupling in magic-angle twisted bilayer graphene,” (2023), [arXiv:2303.14903 \[cond-mat.mes-hall\]](#).

- [62] R. Samajdar, M. S. Scheurer, S. Turkel, C. Rubio-Verdú, A. N. Pasupathy, J. W. F. Venderbos, and R. M. Fernandes, “Electric-field-tunable electronic nematic order in twisted double-bilayer graphene,” *2D Materials* **8**, 034005 (2021).
- [63] L. Zou, H. C. Po, A. Vishwanath, and T. Senthil, “Band structure of twisted bilayer graphene: Emergent symmetries, commensurate approximants, and wannier obstructions,” *Phys. Rev. B* **98**, 085435 (2018).
- [64] M. S. Scheurer, D. F. Agterberg, and J. Schmalian, “Selection rules for cooper pairing in two-dimensional interfaces and sheets,” *npj Quantum Materials* **2**, 9 (2017).
- [65] S. Yip and A. Garg, “Superconducting states of reduced symmetry: General order parameters and physical implications,” *Phys. Rev. B* **48**, 3304 (1993).
- [66] R. Bistritzer and A. H. MacDonald, “Moiré bands in twisted double-layer graphene,” *Proceedings of the National Academy of Sciences* **108**, 12233 (2011).
- [67] D. M. Basko and I. L. Aleiner, “Interplay of Coulomb and electron-phonon interactions in graphene,” *Phys. Rev. B* **77** (2008), 10.1103/physrevb.77.041409.
- [68] D. M. Basko and I. L. Aleiner, “Interplay of coulomb and electron-phonon interactions in graphene,” *Phys. Rev. B* **77**, 041409 (2008).
- [69] B. Putzer, M. Christos, and M. S. Scheurer, “In preparation,” (2023).
- [70] C.-X. Liu, Y. Chen, A. Yazdani, and B. A. Bernevig, “Electron-K-Phonon Interaction In Twisted Bilayer Graphene,” arXiv e-prints (2023), 2303.15551 [cond-mat.supr-con].
- [71] M. S. Scheurer, *Mechanism, symmetry and topology of ordered phases in correlated systems*, Ph.D. thesis, Karlsruhe Institut für Technologie (KIT) (2016).
- [72] E. I. Timmons, S. Teknowijoyo, M. Kończykowski, O. Cavani, M. A. Tanatar, S. Ghimire, K. Cho, Y. Lee, L. Ke, N. H. Jo, S. L. Bud’ko, P. C. Canfield, P. P. Orth, M. S. Scheurer, and R. Prozorov, “Electron irradiation effects on superconductivity in PdTe_2 : An application of a generalized anderson theorem,” *Phys. Rev. Res.* **2**, 023140 (2020).
- [73] E. Khalaf, A. J. Kruchkov, G. Tarnopolsky, and A. Vishwanath, “Magic angle hierarchy in twisted graphene multilayers,” *Phys. Rev. B* **100** (2019), 10.1103/physrevb.100.085109.

Appendix A: Normal-state

1. Parallel and anti-parallel spins

We first discuss in more detail the spin structure of the superconducting states and the meaning of the symmetries of the effectively spinless bands, used in the main text to classify the superconducting states. We distinguish the two cases of (i) parallel spins in the two valleys and (ii) anti-parallel spins. To understand the physical meaning of the spinless symmetries of the main text, we start by listing the symmetries and their representations on the continuum-model operators $\psi_{\rho,\ell,\eta,s}(\mathbf{r})$ and band-operators $d_{\mathbf{k},\alpha,\eta,s}$ before normal-state polarization, where ρ, ℓ, η, s , and α are indices for the sublattice, layer, valley, spin, and the two flat bands, while ρ_j, η_j, s_j , and σ_j are Pauli matrices in sublattice, valley, spin, and band space, respectively:

1. Two-fold rotation along z , C_{2z} : $\psi(\mathbf{r}) \rightarrow \eta_x \rho_x \psi(-\mathbf{r})$ and $d_{\mathbf{k}} \rightarrow \eta_x d_{-\mathbf{k}}$
2. Spinless time-reversal, Θ : $\psi(\mathbf{r}) \rightarrow \eta_x \psi(\mathbf{r})$ and $d_{\mathbf{k}} \rightarrow \eta_x d_{-\mathbf{k}}$
3. Spinful time-reversal, Θ_s : $\psi(\mathbf{r}) \rightarrow \eta_x i s_y \psi(\mathbf{r})$ and $d_{\mathbf{k}} \rightarrow \eta_x i s_y d_{-\mathbf{k}}$
4. SO(3) spin-rotations, $R_s(\boldsymbol{\varphi})$: $\psi(\mathbf{r}) \rightarrow e^{i\boldsymbol{\varphi} \cdot \mathbf{s}/2} \psi(\mathbf{r})$ and $d_{\mathbf{k}} \rightarrow e^{i\boldsymbol{\varphi} \cdot \mathbf{s}/2} d_{\mathbf{k}}$
5. Global U(1) gauge symmetry, $U(\phi)$: $\psi(\mathbf{r}) \rightarrow e^{i\phi} \psi(\mathbf{r})$ and $d_{\mathbf{k}} \rightarrow e^{i\phi} d_{\mathbf{k}}$
6. Three-fold rotation along z , C_{3z} : $\psi(\mathbf{r}) \rightarrow e^{i\frac{2\pi}{3}\rho_z\eta_z} \psi(C_{3z}\mathbf{r})$ and $d_{\mathbf{k}} \rightarrow d_{C_{3z}\mathbf{k}}$
7. Two-fold rotation along x , C_{2x} : $\psi(\mathbf{r}) \rightarrow \rho_x \psi(C_{2x}\mathbf{r})$ and $d_{\mathbf{k}} \rightarrow \sigma_z d_{C_{2x}\mathbf{k}}$

Except for Θ_s and Θ , which are anti-linear, all representations are linear. In case (i) and assuming for concreteness that the active bands at the Fermi level of the flat bands are entirely spin-up ($s = \uparrow$), we simply define the fermionic operators of the main text as

$$c_{\mathbf{k},\alpha,\eta} := d_{\mathbf{k},\alpha,\eta,\uparrow}. \quad (\text{A1})$$

The remaining (non-trivial) symmetries then act as $C_{2z} : c_{\mathbf{k}} \rightarrow \eta_x c_{-\mathbf{k}}$, $\Theta : c_{\mathbf{k}} \rightarrow \eta_x c_{-\mathbf{k}}$, $U(\phi) : c_{\mathbf{k}} \rightarrow e^{i\phi} c_{\mathbf{k}}$, $C_{3z} : c_{\mathbf{k}} \rightarrow c_{C_{3z}\mathbf{k}}$, and $C_{2x} : c_{\mathbf{k}} \rightarrow \sigma_z c_{C_{2x}\mathbf{k}}$, exactly as in the main text.

The situation is more non-trivial in case (ii). Let us assume, for notational simplicity, that the spin polarization of the active flat bands in valley $\eta = +$ is $s = \uparrow$ and in valley $\eta = -$ is \downarrow . Accordingly, we define

$$c_{\mathbf{k},\alpha,+} := d_{\mathbf{k},\alpha,+, \uparrow}, \quad c_{\mathbf{k},\alpha,-} := d_{\mathbf{k},\alpha,-, \downarrow}, \quad (\text{A2})$$

as the effectively spinless fermionic operators used in the main text. It clearly holds, exactly as before, $U(\phi) : c_{\mathbf{k}} \rightarrow e^{i\phi} c_{\mathbf{k}}$, $C_{3z} : c_{\mathbf{k}} \rightarrow c_{C_{3z}\mathbf{k}}$, and $C_{2x} : c_{\mathbf{k}} \rightarrow \sigma_z c_{C_{2x}\mathbf{k}}$. However, Θ and C_{2z} are explicitly broken and, thus, have to be replaced by appropriate combinations with other symmetries. Let us define

$$\tilde{\Theta} := U(-\pi/2)\Theta_s R_s(\pi\hat{e}_z), \quad \tilde{C}_{2z} := U(-\pi/2)C_{2z}R_s(\pi\hat{e}_x), \quad (\text{A3})$$

which are symmetries of the system and obey the same algebraic relations as the symmetries in the main text,

$$\tilde{\Theta}^2 = \tilde{C}_{2z}^2 = \mathbb{1}, \quad [\tilde{\Theta}, \tilde{C}_{2z}] = 0, \quad [\tilde{\Theta}, C_{2x}] = [\tilde{\Theta}, C_{3z}] = [\tilde{C}_{2z}, C_{2x}] = [\tilde{C}_{2z}, C_{3z}] = 0. \quad (\text{A4})$$

In fact, their representation on the fermions defined in Eq. (A2) is exactly the same as that of Θ and C_{2z} in the main text, $\tilde{C}_{2z} : c_{\mathbf{k}} \rightarrow \eta_x c_{-\mathbf{k}}$ and $\tilde{\Theta} : c_{\mathbf{k}} \rightarrow \eta_x c_{-\mathbf{k}}$. As such, for case (ii), the time-reversal symmetry Θ and two-fold-rotational symmetry C_{2z} in the main text can be identified with $\tilde{\Theta}$ and \tilde{C}_{2z} in Eq. (A3). To illustrate this further and also explicitly discuss the spin structure of the order parameter, we transform the superconducting order parameter back to the d -fermions via Eq. (A2),

$$\mathcal{H}_p = \sum_{\mathbf{k}} c_{\mathbf{k},\alpha,+}^\dagger (\Delta_{\mathbf{k}})_{\alpha,\alpha'} c_{-\mathbf{k},\alpha',-}^\dagger = \frac{1}{2} \sum_{\mathbf{k}} d_{\mathbf{k},\alpha,+}^\dagger [(s_0 + s_z)is_y]_{s,s'} (\Delta_{\mathbf{k}})_{\alpha,\alpha'} d_{-\mathbf{k},\alpha',-,s'}^\dagger, \quad (\text{A5})$$

which shows that we obtain an admixture of singlet and (unitary) triplet pairing. To demonstrate the action of $\tilde{\Theta}$ and \tilde{C}_{2z} more explicitly and provide a consistency check, let us focus on $\Delta_{\mathbf{k}} = 2\Delta\sigma_y$, where Eq. (A5) becomes

$$\mathcal{H}_p = \frac{\Delta}{2} \sum_{\mathbf{k}} d_{\mathbf{k}}^\dagger (is_0\eta_y + s_z\eta_x)is_y\sigma_y d_{-\mathbf{k}}^\dagger. \quad (\text{A6})$$

From Eq. (A3), we find the representations $\tilde{C}_{2z} : d_{\mathbf{k}} \rightarrow \eta_x s_x d_{-\mathbf{k}}$ and $\tilde{\Theta} : d_{\mathbf{k}} \rightarrow \eta_x s_x d_{-\mathbf{k}}$; applying this in Eq. (A6), we find that

$$\tilde{C}_{2z} : \Delta \rightarrow \Delta, \quad \tilde{\Theta} : \Delta \rightarrow -\Delta^*, \quad (\text{A7})$$

exactly as in the main text.

For case (i), Eq. (A5) instead becomes

$$\mathcal{H}_p = \sum_{\mathbf{k}} c_{\mathbf{k},\alpha,+}^\dagger (\Delta_{\mathbf{k}})_{\alpha,\alpha'} c_{-\mathbf{k},\alpha',-}^\dagger = \frac{1}{2} \sum_{\mathbf{k}} d_{\mathbf{k},\alpha,+}^\dagger [(s_x + is_y)is_y]_{s,s'} (\Delta_{\mathbf{k}})_{\alpha,\alpha'} d_{-\mathbf{k},\alpha',-,s'}^\dagger, \quad (\text{A8})$$

i.e., a non-unitary triplet state—as expected [27] since this is the “Hund’s partner” of the singlet-triplet admixed state in Eq. (A5), obtained by an independent spin-rotation in the two valleys $[\text{SU}(2)_- \times \text{SU}(2)_+]$. For $\Delta_{\mathbf{k}} = 2\Delta\sigma_y$ this yields

$$\mathcal{H}_p = \frac{\Delta}{2} \sum_{\mathbf{k}} d_{\mathbf{k}}^\dagger (s_x\eta_x + is_y\eta_x)is_y\sigma_y d_{-\mathbf{k}}^\dagger. \quad (\text{A9})$$

Again in accordance with the spinless formulation of the main text, we get $C_{2z} : \Delta \rightarrow \Delta$ and $\Theta : \Delta \rightarrow -\Delta^*$.

We finally note that the normal-state polarization also determines the spin-structure of the fluctuating orders in Table II and Table III: switching between the two scenarios (i) and (ii) requires replacing an order parameter for the correlated insulator by its “Hund’s partner” (see, e.g., Table II in [13] for a complete list). As the system is believed to be close to the $\text{SU}(2)_- \times \text{SU}(2)_+$ symmetric limit (the intervalley Hund’s coupling was estimated to be smaller than 0.1 meV in [24]), the strength of fluctuations of Hund’s partners is expected to be roughly the same. As such, both scenarios (i) and (ii) are consistent with a mechanism based on fluctuations of an order parameter of a correlated insulator. As mentioned in the main text, this is different for phonons, where only scenario (i) allows for intervalley phonons providing the pairing glue.

2. Hartree-Fock numerics

To capture the non-interacting band structure, we use a continuum-model description [66],

$$\mathcal{H}_0 = \int d\mathbf{r} \psi_{\rho,\ell,\eta,s}^\dagger(\mathbf{r}) [h_\eta(\nabla, \mathbf{r})]_{\rho,\ell;\rho',\ell'} \psi_{\rho',\ell',\eta,s}(\mathbf{r}), \quad (\text{A10})$$

where $\psi_{\rho,\ell,\eta,s}^\dagger$ creates an electron of spin $s = \uparrow, \downarrow$, in valley $\eta = \pm$, sublattice $\rho = A, B$, and with pseudo-layer quantum-number $\ell = 1, 2$; in case of TBG, ℓ refers to the actual two graphene layers, whereas, for TTG, it denotes the two mirror-even layer-eigenstates, $(1, 1, 1)^T$ and $(1, -2, 1)^T$, of the three layers [73]. The continuum model involves two terms, $(h_\eta)_{\ell,\ell'} = \delta_{\ell,\ell'} h_{\ell,\eta}^{(d)}(\nabla) + (h_\eta^{(t)}(\mathbf{r}))_{\ell,\ell'}$; the first one, $h_{\ell,\eta}^{(d)} = -i\hbar v_F e^{i\frac{\rho_z \theta_\ell}{2}} (\eta \rho_x \partial_x - \rho_y \partial_y) e^{-i\frac{\rho_z \theta_\ell}{2}}$ with ρ_j being Pauli matrices in sublattice space, describes the Dirac cones of chirality η , rotated by $\theta_\ell = (-1)^\ell \theta/2$ in the two (pseudo)layers ℓ ; the second one, $h^{(t)}$, captures the tunneling between the layers, with amplitude w_0 and w_1 between the same and opposite sublattices, respectively. The modulation of the tunneling on the moiré scale leads to a reconstruction of the band structure, exhibiting nearly flat bands for magic angles around $\theta \simeq 1.1^\circ$ and $\theta \simeq 1.5^\circ$ for TBG and TTG, respectively. We take $w_1 = 89$ meV, $\frac{w_0}{w_1} = .55$, $v_F = 10^6$ m/s, $\theta = 1.09^\circ$ in all our numerical calculations.

As already mentioned above, experiments [19, 20] indicate that the superconducting phase in the density regime $2 < |\nu| < 3$ coexists with the reset behavior at half-filling, $|\nu| = 2$, of the upper or low flat-bands. To model this effect, we add Coulomb repulsion,

$$\mathcal{H}_C = \frac{1}{2N} \sum_{\mathbf{q}} V(\mathbf{q}) \rho_{\mathbf{q}} \rho_{-\mathbf{q}} \quad (\text{A11})$$

to our Hamiltonian, where $\rho_{\mathbf{q}}$ is the Fourier transform of the density of the continuum-model electrons $c_{\mathbf{r}}$ and the N the number of moiré unit cells. We assume a double gate screened Coulomb potential of the form:

$$V(\mathbf{q}) = \frac{1}{A_m} \frac{1 - e^{-2d_s|\mathbf{q}|}}{2\epsilon\epsilon_0|\mathbf{q}|} \quad (\text{A12})$$

In the above, A_m is the area of a real-space moiré unit cell (since we consider TBG and not TTG in our numerics, we take A_m to be the moiré unit cell for 1.09°), d_s is the screening distance which we take to be 40 nm, and ϵ is the dielectric constant we take to be $\epsilon \simeq 4$. Note that projecting Eq. (A11) into the bands of TTG will also lead to interactions coupling the mirror-sectors. However, as was shown [13] analytically in a specific limit and numerically for realistic parameters, also the interacting physics of TTG decays into that of the TBG and that of a single Dirac cone for $D_0 = 0$. As such, it is justified to focus on the mirror-bands as in Eq. (A10) when discussing the reset physics in TTG at $D_0 = 0$.

In computing the normal state, we assume the same normal state density matrix as in Ref. 13 where the expectation value $\langle c_{\mathbf{k},\alpha,\eta}^\dagger c_{\mathbf{k},\beta,\eta} \rangle$ is equal to the $\frac{1}{2}\text{Id}$ in the subspace of the flat bands of one spin flavor which are half filled in our normal state and equal to Id in the flat bands of the remaining spin flavor which are fully polarized. We emphasize that we are assuming a static, momentum independent ansatz for the normal state density matrix which is not obtained self consistently. As can be seen in Fig. II, instead of just rigidly shifting one spin species away from the Fermi level, there are also significant band renormalizations, in particular for the active spin flavor. Similar to the toy model with $t' < 0$ used in Fig. 1, the Dirac cones at the K and K' points are pushed towards the top of the bands.

3. Gauge Fixing

We will also describe how we fix the phases of the continuum model Bloch wavefunctions we use in our computations. We denote the wavefunction of band n in valley η at momentum \mathbf{k} by $u_{\mathbf{k},n,\eta}$. We use $C_{2z}\mathcal{T}$ to fix the phase of the wavefunctions to be either +1 or -1 by enforcing:

$$C_{2z}\mathcal{T}u_{\mathbf{k},n,\eta} = u_{\mathbf{k},n,\eta} \quad (\text{A13})$$

We then fix the relative sign of wavefunctions in opposite flat bands but the same valley with the chiral symmetry operator C as:

$$Cu_{\mathbf{k},\pm,\eta} = i\eta \pm u_{\mathbf{k},\mp,\eta} / |\langle u_{\mathbf{k},\mp,\eta}^* | C | u_{\mathbf{k},\pm,\eta} \rangle| \quad (\text{A14})$$

We fix the relative sign of wavefunctions in opposite bands and opposite valleys with PHC_{2z} , where PH a unitary particle hole symmetry operator with:

$$PHC_{2z}u_{\mathbf{k},\pm,\eta} = \pm\eta u_{\mathbf{k},\mp,-\eta} \quad (\text{A15})$$

Finally, we use time-reversal symmetry to fix the relative sign between wavefunctions at opposite \mathbf{k} , in opposite valleys, but within the same band:

$$\mathcal{T}u_{\mathbf{k},n,\eta} = u_{-\mathbf{k},n,-\eta} \quad (\text{A16})$$

Appendix B: Gap Equation at $T = 0$

In this appendix we will discuss the self consistency equations we solve to obtain our $T = 0$ solutions. In general, we write the Hamiltonian in a Nambu basis as:

$$\mathcal{H}_{\mathbf{k}} = \begin{pmatrix} c_{\mathbf{k},+}^\dagger & c_{-\mathbf{k},-} \end{pmatrix} \begin{pmatrix} \xi_{\mathbf{k},+} & \Delta(\mathbf{k}) \\ \Delta(\mathbf{k})^\dagger & -\xi_{-\mathbf{k},-} \end{pmatrix} \begin{pmatrix} c_{\mathbf{k},+} \\ c_{-\mathbf{k},-}^\dagger \end{pmatrix} \quad (\text{B1})$$

Where we have suppressed spin and band indices, and both $\xi_{\mathbf{k},\pm}$ and $\Delta_{\mathbf{k}}$ are matrices in band and spin space. $\xi_{\mathbf{k},\pm}$ represents the normal state dispersion in the \pm valleys, which we take to be spin polarized and renormalized by Coulomb interactions as described in App. A. $\Delta_{\mathbf{k}}$ can be expressed as:

$$\Delta_{\mathbf{k}}^{\alpha,\eta;\beta,-\eta} = \frac{1}{N} \sum_{\mathbf{k},\mathbf{k}'} \chi_{\mathbf{k},\mathbf{k}'} \lambda_{\mathbf{k},\mathbf{k}'}^{\alpha,\eta;\gamma,\eta'} (\langle c_{-\mathbf{k}} c_{\mathbf{k}} \rangle^T)^{\gamma,\eta';\delta,-\eta'} \left(\lambda_{-\mathbf{k},\mathbf{k}'}^T \right)^{\delta,-\eta';\beta,-\eta} \quad (\text{B2})$$

In the above, $\lambda_{\mathbf{k},\mathbf{k}'}^{\alpha,\eta;\gamma,\eta'}$ represent form factors of some matrix elements which could represent either phonons or fluctuations projected into the flat bands and may be valley diagonal or off diagonal. $V_{\mathbf{k},\mathbf{k}'}$ is an isotropic potential which we will generally take to be attractive and flat for phonons and attractive with some lorentzian form for fluctuation mediated pairing. Since we will be assuming interactions with strength less than the scale of the coulomb interactions, we will treat the polarized spin flavor which is fully occupied at $\nu = 2$ as a spectator and assume the pairing is zero in these bands. The self consistency condition we solve at $T = 0$ is:

$$\langle c_{-\mathbf{k},\alpha,-} c_{\mathbf{k},\beta,+} \rangle = U_{\mathbf{k}}^* \chi_{\mathbf{k}} U_{\mathbf{k}}^T \quad (\text{B3})$$

Where $U_{\mathbf{k}}$ is defined as the unitary operator such that:

$$U_{\mathbf{k}}^\dagger \mathcal{H}_{\mathbf{k}} U_{\mathbf{k}} = D_{\mathbf{k}} \quad (\text{B4})$$

Here, $D_{\mathbf{k}}$ is a diagonal matrix with the Fermi-Dirac functions of eigenvalues of $\mathcal{H}_{\mathbf{k}}$ at $T = 0$ as its diagonal entries. $\chi_{\mathbf{k}}$ is the matrix with Fermi-Dirac functions at $T = 0$ K of the entries of D on the diagonal. We also must impose Fermi-Dirac statistics as a constraint on our solutions. We enforce this constraint at each iteration by splitting $\langle c_{-\mathbf{k},\alpha,-} c_{\mathbf{k},\beta,+} \rangle$ into components which go as either η_x in valley space (denoted $E_{\mathbf{k}}$) or η_y in valley space (denoted as $O_{\mathbf{k}}$) depending on whether the pairing is even or odd under $\mathbf{k} \rightarrow -\mathbf{k}$ and the antisymmetry or symmetry of the band indices as:

$$O_{\mathbf{k}} = \frac{1}{2} (\langle c_{-\mathbf{k},\alpha,-} c_{\mathbf{k},\beta,+} \rangle + \langle c_{\mathbf{k},\beta,-} c_{-\mathbf{k},\alpha,+} \rangle) \quad E_{\mathbf{k}} = \frac{1}{2} (\langle c_{-\mathbf{k},\alpha,-} c_{\mathbf{k},\beta,+} \rangle - \langle c_{\mathbf{k},\beta,-} c_{-\mathbf{k},\alpha,+} \rangle) \quad (\text{B5})$$

Our iterative procedure then proceeds as follows. At the zeroth iteration, an ansatz for $\langle c_{-\mathbf{k},\alpha,-} c_{\mathbf{k},\beta,+} \rangle$ satisfying the desired symmetries is selected. Then at each iteration, the chemical potential is adjusted to give the desired filling, which we take to be $\nu = 2.5$ in our numerics. $U_{\mathbf{k}}$ and the resulting functions $O_{\mathbf{k}}$ and $E_{\mathbf{k}}$ are then computed and plugged back into $\Delta_{\mathbf{k}}$, (which also is guaranteed to obey Fermi-Dirac statistics assuming our generalized form factors obey time reversal symmetry). $\Delta_{\mathbf{k}}$ is then used to compute the new $U_{\mathbf{k}}$, and the procedure is repeated until convergence is reached in $\Delta_{\mathbf{k}}$ and μ . In practice, in our $T = 0$ numerics, we take $\mathbf{q} = \mathbf{k} - \mathbf{k}'$ to only be summed over the first Brillouin zone when we consider fluctuation mediated superconductivity, an assumption justified for our fluctuation mediated SC by $\chi(\mathbf{q})$ falling off as $\frac{1}{|\mathbf{q}|^2}$ near the first Brillouin zone edge. For phonon mediated superconductivity, we include an additional shell of the 6 nearest Brillouin zones in our sum over \mathbf{q} . Including more shells may reduce the needed coupling, though we expect the leading instability of A_1 phonons should be unchanged.

TABLE III: Generalization of Table II of the main text, where we also indicate the dominant superconducting orders ($\bar{\Delta}$) in the microscopic basis, obtained by applying Eq. (7) in the sublattice basis. The phonon modes refer to the sublattice-basis form $\bar{\lambda}_j$ of the coupling, cf. Eq. (8), and “g-nematic” stands for the (intravalley) graphene nematic state of Ref. 62, which has the same coupling as the E_2 phonon.

Fluctuating Order			Leading SC (band)		Leading SC (microscopic)	
type	λ^j	$\bar{\lambda}^j$	$\Delta_{\mathbf{k},\eta}$	IR	$\bar{\Delta}_{\mathbf{k},\eta}$	IR
T-IVC/ A_1, B_1 phonon	$\sigma_0 \eta_{x,y}$	$\rho_x \eta_{x,y}$	$\sigma_y \delta_{\mathbf{k}}$	A_2	$\rho_z \eta \delta_{\mathbf{k}}$	A_2
K-IVC	$\sigma_y \eta_{x,y}$	$\rho_y \eta_{x,y}$	$\sigma_0 \eta \delta_{\mathbf{k}}$	B_1	$\rho_0 \eta \delta_{\mathbf{k}}$	B_1
SLP+	$\sigma_y \eta_z$	$\rho_z \eta_0$	$\sigma_y \delta_{\mathbf{k}}, \sigma_0 \eta \delta_{\mathbf{k}}$	A_2, B_1	$\rho_z \eta \delta_{\mathbf{k}}, \rho_0 \eta \delta_{\mathbf{k}}$	A_2, B_1
SLP−	$\sigma_y \eta_0$	$\rho_z \eta_z$	$\sigma_x \eta \delta_{\mathbf{k}}, \sigma_z \eta \delta_{\mathbf{k}}$	B_2, B_1	$(\rho_y, \rho_x \eta)$	E_1
N-IVC	—	$\eta_{x,y} \rho_{0,z}$	—	—	$(\rho_y, \rho_x \eta)$	E_1
g-nematic/ E_2 phonon	—	$(\eta_z \rho_y, -\rho_x)$	—	—	$\rho_0 \eta \delta_{\mathbf{k}}$	B_1

Appendix C: Linearized Gap Equation at T_c

In this appendix, we will describe how we compute solutions to the linearized gap equation at T_c . As in App. B, we will assume a spin polarized normal state and only consider superconducting instabilities within a single spin flavor. We recall that for the case of fluctuation-mediated superconductivity, we couple electrons to bosonic modes ($j = 1, 2, \dots$) as, e.g., in Eq. (4), with $\lambda_{\alpha,\eta;\alpha',\eta'}^j$ capturing the symmetries broken by the corresponding order parameter. In order to compactly write down the linearized gap equation, it is convenient to express λ^j as

$$\left(\lambda_{\alpha,\eta;\alpha',\eta'}^j\right)_{\mathbf{k},\mathbf{k}'} = A_{\mathbf{k},\mathbf{k}'}^{\alpha,\eta;\alpha',-\eta} \delta_{\eta,-\eta'} + B_{\mathbf{k},\mathbf{k}'}^{\alpha,\eta;\alpha',\eta} \delta_{\eta,\eta'}. \quad (\text{C1})$$

Here we also include the momentum dependence of the matrix elements, which arises when we study phonons and order parameter fluctuations projected from the sublattice basis to the band basis. In Eq. (C1), $A_{\mathbf{k},\mathbf{k}'}$ are the valley off diagonal pieces of the form factor $\lambda_{\alpha,\eta;\alpha',\eta'}^j$ and $B_{\mathbf{k},\mathbf{k}'}$ is the valley diagonal pieces. With this notation in hand, the linearized gap equation we solve is

$$(\Delta(\mathbf{k})^\dagger)^{\alpha,-;\beta+} = \sum_{\mathbf{q}} \chi_{\mathbf{q}} \left(\mathcal{G}_{\mathbf{k}-\mathbf{q}}^{\delta-;\gamma+} B_{\mathbf{k}-\mathbf{q},\mathbf{q}}^{\gamma+;\beta+} (B_{-\mathbf{k}+\mathbf{q},-\mathbf{q}}^T)^{\alpha-;\delta-} - \mathcal{G}_{-\mathbf{k}+\mathbf{q}}^{\gamma-;\delta+} A_{\mathbf{k}-\mathbf{q},\mathbf{q}}^{\gamma-;\beta+} (A_{-\mathbf{k}+\mathbf{q},-\mathbf{q}}^T)^{\alpha-;\delta+} \right), \quad (\text{C2})$$

where the Greens function $\mathcal{G}_{\mathbf{k}-\mathbf{q}}^{\alpha+;\beta-}$ defined by

$$\mathcal{G}_{\mathbf{k}}^{\alpha+;\beta-} = \frac{1}{2A_m} \left(\frac{\Delta_{\mathbf{k}}^{00}}{2|\xi_{\mathbf{k},0}|} (1 - 2n_F(|\xi_{\mathbf{k},0}|)) (\sigma_0 + \sigma_z)^{\alpha\beta} + \frac{\Delta_{\mathbf{k}}^{11}}{2|\xi_{\mathbf{k},1}|} (1 - 2n_F(|\xi_{\mathbf{k},1}|)) (\sigma_0 - \sigma_z)^{\alpha\beta} + \frac{\Delta_{\mathbf{k}}^{01}}{\xi_{\mathbf{k},0} + \xi_{\mathbf{k},1}} (n_F(-\xi_{\mathbf{k},1}) - n_F(\xi_{\mathbf{k},0})) (\sigma_x + i\sigma_y)^{\alpha\beta} + \frac{\Delta_{\mathbf{k}}^{10}}{\xi_{\mathbf{k},0} + \xi_{\mathbf{k},1}} (n_F(-\xi_{\mathbf{k},1}) - n_F(\xi_{\mathbf{k},0})) (\sigma_x - i\sigma_y)^{\alpha\beta} \right). \quad (\text{C3})$$

Here $\Delta_{\mathbf{k}}^{\alpha\beta}$ denote the pairing in band space where $\alpha, \beta = 0, 1$ label the upper and lower flat band. Finding a solution to the above equation then amounts to computing the right-hand side of Eq. (C2), diagonalizing it in the space of momenta, Nambu index, and band index, and looking at the eigenvectors which attain eigenvalue 1 for some value of T . To enforce Fermi-Dirac statistics, we solve the above equation on half of the moiré Brillouin zone. We also exclude the edge points in our linearized gap equation computations for phonons and projected order fluctuations. We expect including these points would reduce the needed coupling to obtain a finite T_c (or reduce T_c for fixed coupling) but not change the leading instabilities.

Appendix D: Additional statements about superconductivity and phonons

1. Generalization to sublattice basis

Due to the basis independent form of the (anti)commutator relation in Eq. (7), it can be readily applied in any basis. As we also study in the numerics of the main text momentum-independent coupling matrices $\bar{\lambda}_j$ in the microscopic sublattice basis, it seems natural to also apply the commutator relation in that basis. Upon noting that the additional projection onto the flat bands does, in general, not commute with the order parameters, it is clear that applying Eq. (7) can only provide approximate guidance even in the strict flat-band limit. Notwithstanding these approximations, the results, summarized in Table III, agree well with the numerics shown in Fig. 4 of the main text. In the case of N-IVC fluctuations, the listed E_1 superconductor is the option where the highest number of components obey Eq. (7), while all components obey it in all other cases.

2. Electron phonon coupling in TTG

As it exhibits three layers, the discussion of the layer structure of the phonon modes in TTG requires additional comments. Starting from uncoupled optical A_1 , B_1 , and E_2 phonons in the three layers of TTG, we can decompose each of these modes into two mirror-even ($\mu = e_1, e_2$) and one mirror-odd ($\mu = o$) contributions,

$$\mathbf{v}_{e_1} = \frac{1}{\sqrt{3}} \begin{pmatrix} 1 \\ 1 \\ 1 \end{pmatrix}, \quad \mathbf{v}_{e_2} = \frac{1}{\sqrt{6}} \begin{pmatrix} 1 \\ -2 \\ 1 \end{pmatrix}, \quad \mathbf{v}_o = \frac{1}{\sqrt{2}} \begin{pmatrix} 1 \\ 0 \\ -1 \end{pmatrix}. \quad (\text{D1})$$

Upon projection into the mirror-even electronic sectors, forming the relevant low-energy flat-band degrees of freedom, the mode \mathbf{v}_o vanishes completely (due to mirror-symmetry), while the first two survive. Their respective projected coupling is of the form of Eq. (8) with $\mathbf{v}_{e_1} = (1, 1)^T/\sqrt{3}$ and $\mathbf{v}_{e_2} = (1, -2)^T/\sqrt{6}$.

3. Electron-phonon matrix elements

In this appendix, we analyze the momentum-independent terms of the electron-phonon coupling matrices $\lambda_{\mathbf{k}, \alpha, \eta; \mathbf{k}', \alpha', \eta'}^{g, j, \mu}$ in Eq. (9). As a result of C_{3z} symmetry, the coupling terms of E_2 cannot have a momentum-independent component and so we focus on $g = A_1, B_1$. Let us expand in Pauli matrices in band and valley space,

$$\lambda_{\mathbf{k}, \alpha, \eta; \mathbf{k}', \alpha', \eta'}^{g, \mu} = \sum_{j_1, j_2} c_{j_1, j_2}^{g, \mu} (\sigma_{j_1})_{\alpha, \alpha'} (\eta_{j_2})_{\eta, \eta'} + \mathcal{O}(\mathbf{k}, \mathbf{k}'), \quad (\text{D2})$$

where Hermiticity implies $c_{j_1, j_2}^{g, \mu} \in \mathbb{R}$. The combination of $U(1)_v$ (valley-charge conservation), C_{2z} , and Θ implies that only $c_{j_1, x}^{A_1, \mu}$, $c_{j_1, y}^{B_1, \mu}$, $j_1 = 0, x, z$ can be non-zero. Chiral symmetry C has the representation ρ_z and $\eta_z \sigma_y$ in the sublattice and band basis, respectively. As ρ_z anti-commutes with both $\Lambda_{A_1} = \eta_x \rho_x$ and $\Lambda_{B_1} = \eta_y \rho_x$, their band projections in Eq. (D2) also have to anti-commute with $\eta_z \sigma_y$; this leaves us with $c_{0, x}^{A_1, \mu}$ and $c_{0, y}^{B_1, \mu}$ as the only non-zero terms. Furthermore, the unitary particle-hole symmetry P anti-commutes with the layer-even ($\mu = +$) and commutes with the layer-odd ($\mu = -$) modes. Being represented by $-i\eta_z \sigma_y$, this is inconsistent with $c_{j_1, x}^{A_1, -}, c_{j_1, y}^{B_1, -} \neq 0$, which thus have to vanish. This is in line with our numerics, where we find very small projections of the layer-odd A_1 and B_1 modes. Their layer-even counterparts, however, are consistent with P if only $c_{0, x}^{A_1, \mu}$ and $c_{0, y}^{B_1, \mu}$ are non-zero. Taken together, we find

$$\lambda_{\mathbf{k}, \alpha, \eta; \mathbf{k}', \alpha', \eta'}^{g, -} = \mathcal{O}(\mathbf{k}, \mathbf{k}'), \quad g = A_1, B_1, \quad \lambda_{\mathbf{k}, \alpha, \eta; \mathbf{k}', \alpha', \eta'}^{A_1, +} = \sigma_0 \eta_x + \mathcal{O}(\mathbf{k}, \mathbf{k}'), \quad \lambda_{\mathbf{k}, \alpha, \eta; \mathbf{k}', \alpha', \eta'}^{B_1, +} = \sigma_0 \eta_y + \mathcal{O}(\mathbf{k}, \mathbf{k}'). \quad (\text{D3})$$

Appendix E: Pairing for other normal-state orders

In the main text, we have discussed pairing in the case of a spin polarized or spin-valley locked normal state. We here comment on the consequences for superconductivity for two other, plausible normal-state scenarios.

1. T-IVC & SP order

Given the current insights from experiment, the most natural alternative scenario is that the normal state exhibits both T-IVC [7] and spin polarization [24, 28] simultaneously. The projection to the remaining two active flavor degrees of freedom is given by

$$P_{\nu=2} = \frac{1}{4} (1 + s_z) (1 + \eta_x \rho_x). \quad (\text{E1})$$

Increasing ν beyond $\nu = 2$ will lead to a metallic state with two non-degenerate bands $\alpha = \pm$ coming from the original flat-band manifold. Let us denote the associated creation operators by $c_{\mathbf{k},\alpha}^\dagger$, which have one index less than the associated operators discussed in the main text since valley is not a good quantum number anymore. The superconducting order parameter is a 2×2 matrix, coupling to the electrons as $\sum_{\mathbf{k},\alpha,\alpha'} c_{\mathbf{k},\alpha}^\dagger (\Delta_{\mathbf{k}})_{\alpha,\alpha'} c_{-\mathbf{k},\alpha'}^\dagger + \text{H.c.}$, and thus has to obey $\Delta_{\mathbf{k}} = -\Delta_{-\mathbf{k}}^T$. As the projector in Eq. (E1) commutes with C_{2z} (in fact, also with C_{2x} and C_{3z}), all pairing states must still be either even or odd under C_{2z} (transform under one of the IRs of D_6 or C_6). Since Eq. (E1) projects onto the subspace where $\eta_x \rho_x$ is -1 , it holds $C_{2z}: c_{\mathbf{k},\alpha}^\dagger \rightarrow -c_{-\mathbf{k},\alpha}^\dagger$ and, hence,

$$C_{2z}: \Delta_{\mathbf{k}} \longrightarrow \Delta_{-\mathbf{k}} = -\Delta_{\mathbf{k}}^T, \quad (\text{E2})$$

which is the analogue of Eq. (2) of the main text. As before, all C_{2z} -even states must be entirely band-off-diagonal, $\Delta_{\mathbf{k}} = \delta_{\mathbf{k}} \sigma_y$. However, since the number of active degrees of freedom is reduced, there are more restrictions: all C_{2z} -odd superconductors must have zeros in the Brillouin zone due to $\Delta_{\mathbf{k}} = -\Delta_{-\mathbf{k}}^T = -\Delta_{-\mathbf{k}}$.

For completeness and to conveniently address energetics, we extend the discussion to the microscopic sublattice basis. Let $\bar{\Delta}_{\mathbf{k}}$ be the corresponding superconducting order parameter—an 8×8 matrix in sublattice, valley, and spin space. Then pairings are constrained to obey

$$P_{\nu=2} \bar{\Delta}_{\mathbf{k}} s_y \eta_x P_{\nu=2}^T = \bar{\Delta}_{\mathbf{k}} s_y \eta_x. \quad (\text{E3})$$

The order parameters which are compatible with Eq. (E3) will all be spin triplets. The C_{2z} -even states, i.e., order parameters transforming under A_2 , E_2 , or A_1 , will have the form (suppressing \mathbf{k} -dependencies) $\bar{\Delta}_{\mathbf{k}} \sim P_{\nu=2} s_x \eta_z \rho_z$; in line with our symmetry arguments above, one can check that they will go as σ_y in band space and thus be purely band off diagonal in the subspace defined by $P_{\nu=2}$. The pairings which are odd under C_{2z} include the B_1 and B_2 pairings with $\bar{\Delta}_{\mathbf{k}} \sim P_{\nu=2} s_x \rho_0$, and E_1 pairings with $\bar{\Delta}_{\mathbf{k}} \sim P_{\nu=2} s_x (\rho_x, \rho_y \eta_z)$ previously discussed in our main text; however, as pointed out above and unlike in the main text, the C_{2z} -odd pairings in both the band basis and sublattice basis are no longer allowed to have a component without a sign change since only the momentum odd components of the B_1 , B_2 , and E_2 pairings survive projection $P_{\nu=2}$.

Since only the band-off-diagonal A_2 state can have a non-sign-changing order parameter, a superconducting state satisfying the criterion around Eq. (7) of the main text can only be this state (or none). We have studied which of the pairing mechanisms survive the projection and whether they favor or disfavor A_2 pairing, see Table IV. We find that A_1 phonons, T-IVC fluctuations, and spin fluctuations all provide an attractive pairing potential, and if any of these have large enough couplings to overcome the normal state band splitting, the A_2 triplet pairing is the leading instability, as in the main text. Furthermore, due to the fact that the remaining bands after reconstruction, as described by the projector $P_{\nu=2}$, are not degenerate (there is no remaining spin symmetry to guarantee degeneracy), a Bogoliubov Fermi surface or a fully gapped state and, thus, a transition from nodal to gapped as a function of filling are possible depending on parameters (similar to our discussion in the main text).

$\Delta_{\mathbf{k}}$	IR of D_6	T-IVC/ A_1 phonon $\eta_x \rho_x$	quantum spin Hall $s_z \eta_z \rho_z$	spin polarized s_z	N-IVC $\eta_x (\rho_0, \eta_z \rho_z)$	quantum Hall $\eta_z \rho_z$
$P_{\nu=2} (s_x \eta_z \rho_z \delta_{\mathbf{k}})$	A_2	✓	✗	✓	✗	✗

TABLE IV: We list the possible pairing glues which are compatible with a T-IVC+SP normal state (i.e., the interactions survive projection to the space of the upper T-IVC bands of a single spin flavor). We denote interactions which will generate an attractive interaction for the A_2 pairing with a ✓ and interactions which will generate a repulsive interaction with a ✗.

2. T-IVC normal state

We will now consider a simpler normal state which leaves twice the number of degrees of freedom as the previous normal state we considered. In particular, we can consider a strong coupling T-IVC normal state with projector of

the form:

$$P_{\nu=2} = \frac{1}{2} (1 + \eta_x \rho_x) \quad (E4)$$

In contrast to the case for a normal state with coexisting T-IVC and spin-polarized order, there are now more possible pairing options and singlet pairing is once again possible. We can classify the possibilities as pairings which are triplet, singlet, and by IRs of the point group. We find the possible pairings include triplet A_1 and A_2 pairings and singlet B_1 and B_2 pairings with:

$$\Delta_{\mathbf{k}} \sim P_{\nu=2} s_x \eta_z \rho_z \quad \Delta_{\mathbf{k}} \sim P_{\nu=2} s_0 \eta_z \rho_z \quad (E5)$$

triplet B_1 and B_2 pairings and singlet versions of our A_1 and A_2 states with:

$$\Delta_{\mathbf{k}} \sim P_{\nu=2} s_x \eta_0 \rho_0 \quad \Delta_{\mathbf{k}} \sim P_{\nu=2} s_0 \eta_0 \rho_0 \quad (E6)$$

and triplet E_1 pairing and singlet E_2 pairing with:

$$\Delta_{\mathbf{k}} \sim P_{\nu=2} s_x (\eta_0 \rho_x, \eta_z \rho_y) \quad \Delta_{\mathbf{k}} \sim P_{\nu=2} s_0 (\eta_0 \rho_x, \eta_z \rho_y) \quad (E7)$$

Of the above, the only options which are not enforced to have a sign change are our purely inter-band A_2 triplet pairing, the A_1 singlet pairing, and the E_2 singlet pairing. Since these pairings do not have a sign change, they are the only possible candidates for the criterion around Eq. (7) of the main text and we have enumerated the possible pairing glues for these s-wave states in Table V.

$\Delta_{\mathbf{k}}$	IR of D_6	T-IVC/ A_1 phonon	quantum spin Hall	Spin polarized	N-IVC	quantum Hall
		$\eta_x \rho_x$	$s \eta_z \rho_z$	s	$\eta_x (\rho_0, \eta_z \rho_z)$	$\eta_z \rho_z$
$P_{\nu=2} (s_x \eta_z \rho_z \delta_{\mathbf{k}})$	A_2 (triplet)	✓	✗	✓	✗	✗
$P_{\nu=2} (s_0 \eta_0 \rho_0 \delta_{\mathbf{k}})$	A_1 (singlet)	✓	✓	✗	✓	✗
$P_{\nu=2} (s_0 (\eta_0 \rho_x, \eta_z \rho_y))$	E_2 (singlet)	✓	✗	✗	✓	✓

TABLE V: We list the possible pairing glues which are compatible with a T-IVC normal state (ie the interactions survive projection to the space of the upper spin-degenerate T-IVC bands). We denote interactions which will generate an attractive interaction with a ✓ and interactions which will generate a repulsive interaction with a ✗.

We find in this case that all of the pairing glues which are attractive for our A_2 triplet pairing are also attractive for one of the singlet pairings, except for spin fluctuations. Therefore, we can say that if the pairing is triplet for a spin-degenerate T-IVC normal state, the leading instability is likely to be our A_2 pairing provided the pairing glue interaction is sufficiently strong and spin fluctuations may play an important role in energetically favoring this state. In this case, we expect that the phenomenology of Bogoliubov Fermi surfaces and a nodal to gapped transition as a function of interaction strength will again apply.

Appendix F: More Superconducting Instabilities

In this appendix, we will discuss the superconducting instabilities we find beyond the A_2 and B_1 states shown in Figs. 2 and 3 of the main text and focus on the other leading instabilities we find in the presence of fluctuations of different particle hole orders. For SLP- fluctuations, we find the B_2 state can be favored over the B_1 when the strength of T-IVC fluctuations are on the same order as SLP- fluctuations, as shown in Fig. 4. We show the B_2 state for parameter value $\theta_{fluc.} \simeq \frac{\pi}{4}$ in Fig. 5. For N-IVC fluctuations as well as for SLP- fluctuations, we find the E_2 is the leading instability, as shown in Fig. 6. We show the two components of the E_2 state for parameter value $\theta_{fluc.} \simeq \frac{\pi}{2}$ in Fig. 4.

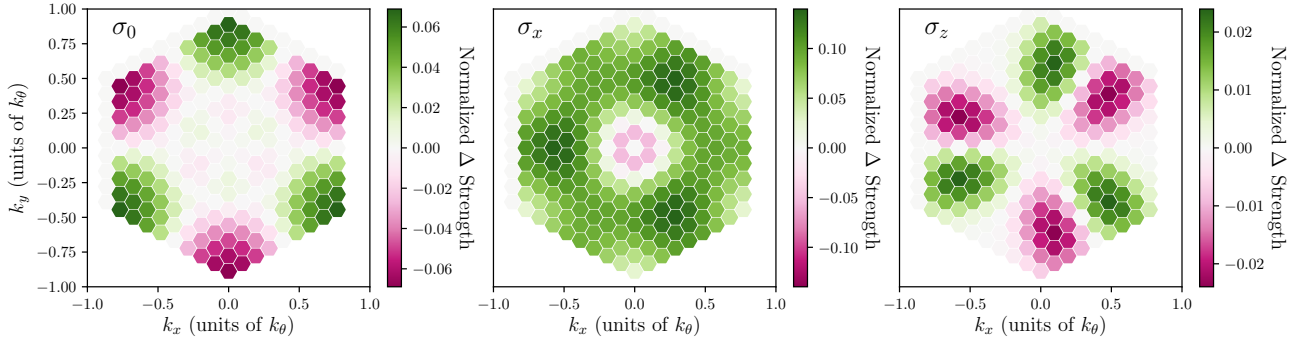


FIG. 5: Highest eigenvalue pairing obtained from linearized gap equation at $T = 16$ K, for SLP- and T-IVC fluctuations. The pairing transforms under the B_2 representation of the point group.

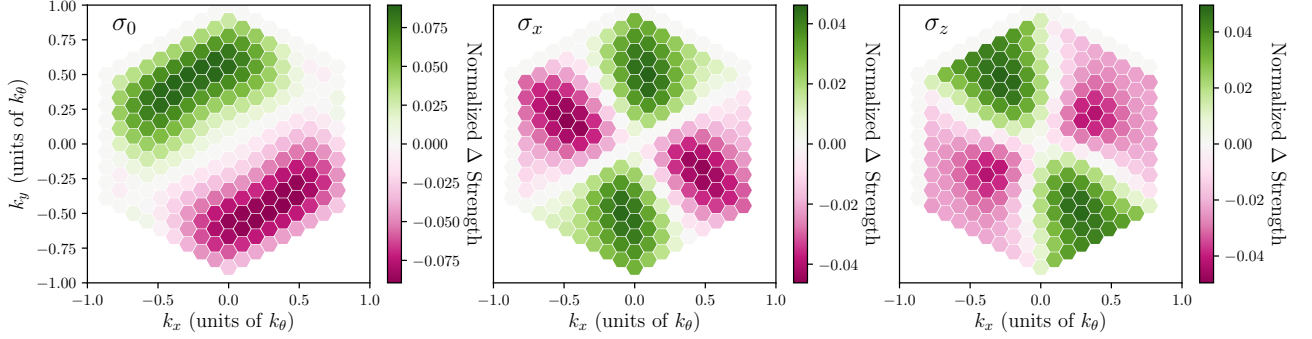


FIG. 6: First component of the highest eigenvalue pairing obtained from linearized gap equation at $T = 16$ K for just N-IVC fluctuations. The pairing transforms under the E_1 representation of the point group. The component shown here is degenerate with the other basis functions which transform under C_3 symmetry shown in Fig. 7.

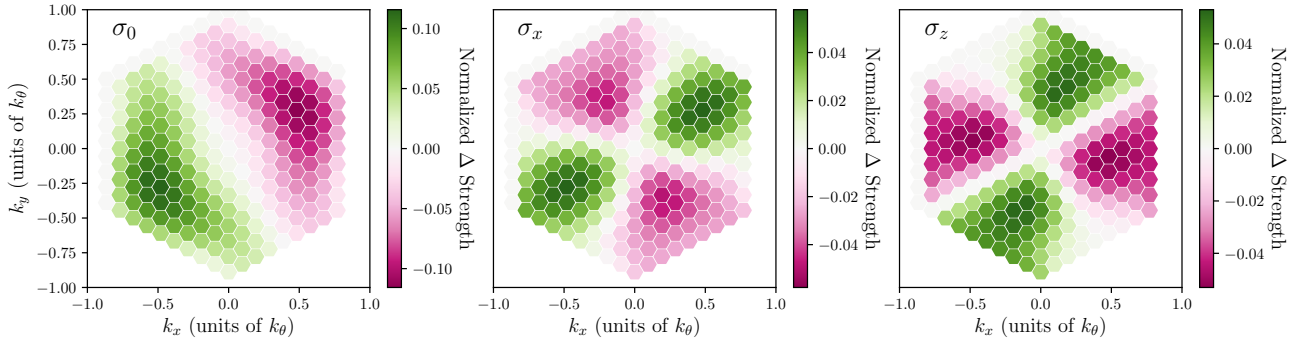


FIG. 7: Second component of the highest eigenvalue pairing obtained from linearized gap equation at $T = 16$ K for just N-IVC fluctuations. The pairing transforms under the E_1 representation of the point group. The component shown here is degenerate with the other basis functions which transform under C_3 symmetry shown in Fig. 6.

We point out that each component of the E_1 pairing shown in Figs. 6 and 7 may by themselves be nodal, assuming the pieces of each pairing which are proportional to σ_x in band space are smaller than the band splitting. In general, we expect the lowest energy pairing at $T = 0$ will be the chiral E_1 state which would be fully gapped; however, in the presence of sufficient strain, a single basis function of the E_1 pairing can be favored over the chiral state, offering another route to nodal superconductivity in the presence of N-IVC fluctuations.